

Unveiling the Importance of Solid–Liquid Interphase for the Development of All Solid-State Sodium Metal Batteries

Rahul Singh, Tushar, Vineeth Sasikumar Kala, Md Osama Zubair, Chhail Bihari Soni, Sungjemmenla, Mahesh Chandra, Kamlesh Kumar, Kundan Kumar Mishra, and Vipin Kumar*

Solid-state sodium batteries (SSSBs) offer high energy density with improved safety, making them an appealing candidate for long-range mobility applications. Considering the advances in SSSBs, ionic conduction is no longer a critical barrier. However, the instability of the electrode/electrolyte interface remains a hurdle, limiting cycling stability and cathode utilization. The compatibility between the electrode/electrolyte is often established by a small amount of liquid/polymer electrolyte. The solid–liquid interphase (SOLI) instead of the solid–solid interface plays a crucial role in deciding the performance of SSSBs. SOLI is a key component of the existing SSSBs, facilitating ion transport while mitigating interfacial resistance. The intricate, but essential, characteristics of SOLI,

namely the composition, distribution, and ionic properties of the interfaces, are highlighted. This review highlights the key design strategies for optimizing the SOLI, including electrolyte engineering, interphase material selection, and the use of multiphase interphases to balance cell performance. Moreover, advanced characterization techniques are discussed, along with recent breakthroughs in SOLI research. This review aims to provide insights into overcoming the challenges of SOLI to enhance the electrochemical performance and long-term stability of SSSBs. A thorough understanding of SOLI engineering will pave the way for practical, safe, and long-lasting high-performance SSSBs.

1. Introduction

With the increased penetration of electric mobility, the demand for high-energy Li-ion batteries has increased. Since more energy is packed into smaller sizes, the high-energy Li-ion batteries pose safety challenges as they comprise flammable liquid electrolytes (LEs).^[1–3] Moving from the flammable LEs to the room-temperature ion-conducting solid-state electrolytes (SSEs) can certainly improve safety. Moreover, the SSEs enable the use of the Li metal anode, which surely increases the cell's energy density.^[4,5] However, the limited availability of the Li and high price per kWh for Li metal batteries may pose a threat to the sustainability of Li metal batteries.^[6–8] On the other hand, the sodium (Na) metal, which shares the chemical and electrochemical properties with Li metal, could be an attractive option for solid-state batteries (SSBs).^[9] The high natural abundance (23000 ppm versus 20 ppm for Li) and relatively high specific capacity (\approx 1166 mAh g⁻¹) of Na metal make it a critical future metal anode and have constantly garnered attention for decades.^[7,10,11]

The central component of any SSB is the SSE that must conduct the mobile ions at ambient conditions. The electrolyte materials with high room-temperature ionic conductivity (0.01–0.1 mS cm⁻¹) are referred to as the “fast ion conductor” or “superionic conductor.” A variety of solid materials have been examined for Na-ion room-temperature conduction. For example, NASICON (Natrium Super Ionic Conductor) is a family of solids ($\text{Na}_{1+y}\text{Zr}_2\text{Si}_y\text{P}_{3-y}\text{O}_{12}$, $0 < y < 3$) that have ionic conductivity of the order of 0.1–3 mS cm⁻¹, comparable to those of LEs (1–10 mS cm⁻¹).^[12,13] In NASICON materials, the ionic movement is primarily caused by the hopping of Na ions among interstitial sites of the crystal lattice.^[14] Alumina (i.e., beta- $\text{Na}_2\text{O}_x\text{Al}_2\text{O}_3$, $5 < x < 11$) solid electrolytes (SEs) are another example of Na ion conductors (\approx 3 mS cm⁻¹) where the Na ion movement occurs in the ionophilic channels of Al_2O_3 .^[15] This material has been widely used in high-temperature Na-sulfur batteries.^[16] Sulfide electrolytes mostly show superior ionic conductivity compared to oxide-based counterparts. This is due to their body-centered cubic (bcc)-like anion sublattice, which significantly enhances Na-ion diffusion. Notably, recent advances in sulfide SEs have yielded ionic conductivities surpassing to those of traditional LEs. Despite the high ionic conductivity and low Na-ion diffusion barrier, most solid-state sodium batteries (SSSBs) have suffered from higher polarization, lower material utilization, limited cycle-life, and low energy density.^[17] Though there could be many reasons for the inferior performance of the SSBs, one of the reasons could be the unstable electrode/electrolyte interface. The interface can easily be disturbed by the physical contact between the electrode and electrolyte if it is not perfect, the presence of grain

R. Singh, M. O. Zubair, C. B. Soni, Sungjemmenla, M. Chandra, K. Kumar, K. K. Mishra, V. Kumar

Department of Energy Science and Engineering
IIT Delhi

Hauz Khas, New Delhi 110016, India
E-mail: vkumar@dese.iitd.ac.in

Tushar, V. Sasikumar Kala, V. Kumar
University of Queensland–IIT Delhi Academy of Research (UQIDAR)
IIT Delhi
Hauz Khas, New Delhi 110016, India

boundaries, or chemical and electrochemical reactions. High interfacial resistance due to poor contact with the Na anode limits ion transport, while slow ionic conductivity at room temperature reduces rate capability.^[18,19] The volume changes during cycling can lead to cracking and delamination at the electrolyte-electrode interfaces, weakening the SE. Moreover, Na dendrites can still penetrate through defects in the SSE, potentially causing short circuits.^[20] Compatibility issues between SEs and electrodes can result in chemical degradation, further deteriorating the stability.^[21] These factors directly or indirectly contribute to premature cell failure. Additionally, the manufacturing of solid-state cells is complex, with challenges in achieving uniform electrolyte thickness and defect-free structures.

Most often, a small amount of liquid or polymer electrolyte is used to activate the solid-electrolyte or to enhance the interfacial ionic transport by mitigating the interfacial resistance.^[22] The liquid interface of the electrode and SE serves as the bridge to compensate for the imperfection of the electrode-electrolyte interface.^[23] This bridge is called the solid-liquid interphase (SOLI) in SSSBs.^[24,25] SOLI is a multifunctional layer that must balance several competing demands, including ion transport, chemical stability, and mechanical properties. The ideal SOLI must prevent Na dendrite growth by smoothing the ionic flux at the interface and accommodating volume changes during cycling. However, several challenges exist in achieving an optimal SOLI. These challenges include the formation of an unstable or nonuniform SOLI, the limited mechanical strength of the interphase, and the potential for continuous electrolyte consumption, leading to cell failure. To overcome these challenges, researchers have explored various strategies, such as tailoring the electrolyte composition with additives, engineering the interphase, and optimizing the mechanical properties of the SOLI to balance stiffness and ductility. These approaches aim to create a stable, conductive, and robust SOLI that can significantly enhance the performance of SSSBs.^[24,25]

Despite growing interest in safety-enabled SSSBs, the critical role of SOLI remains untouched in the literature. A comprehensive understanding of the fundamentals of designing SOLI remains scant. Hence, the present review catalyzes the understanding to bridge the fundamental principles and basics of SOLI with the cell design. It provides a thorough overview of the current understanding of SOLI formation, challenges, and potential solutions. We further examine the design strategies for creating effective SOLIs and

the characterization techniques used to probe their properties and highlight recent advances in research. By offering a focused and forward-looking perspective, we believe that this review guides future research efforts and accelerates the development of safety-enabled SSSBs. Overall, the present work aims to open a fresh and new direction to improve the electrochemical performance and stability of SSSBs. However, the nomenclature related to "all-solid-state batteries" (ASSBs), "quasi-solid-state batteries" (QSSBs), and "semi-solid-state batteries" is complicated and context-dependent. We have used the term "all-solid-state battery" to generically denote systems that utilize SSEs as the principal medium for ion transport. The liquid is nonflowing and discontinuous and does not function as the principal conduction channel. Consequently, we classified this system as part of the broader category of "ASSBs with interfacial modifications," a phrase employed in many recent studies.^[26–28]

2. SOLI in SSE: Basics and Mechanisms

The interface between SSEs and electrode plays a pivotal role in determining the performance and stability of SSSBs. As the components of SSSBs are solid (ideally), this results in the formation of multiple interphases within the battery structure. These interphases include the cathode-electrolyte interphase (CEI), electrolyte-electrolyte interface (EEI) (where multiple electrolyte layers meet, e.g., bilayer or tri-layer), anode-electrolyte interphase, current collector-electrolyte interphase, and additive-electrolyte interphase. Among them, the anode-electrolyte and CEI are critical, since they have a big impact on deciding the capacity, stability, and overall performance of the cell. These interphases influence the vitals of the cell, for instance, ionic or electronic conductivity, charge transfer resistance, and mechanical integrity.^[29]

To mitigate the limitations of direct solid-solid contact, such as poor interfacial wettability, mechanical mismatches, and interfacial resistance, typically, a liquid or polymer interphase modifier is employed to minimize the interfacial resistance. This results in formation of SOLI, which functions as a multifunctional layer facilitating ionic mobility across interface while alleviating mechanical and electrochemical incompatibilities. On the other hand, although conventional LE-based Na metal batteries (SMBs) have the advantage of high ionic conductivity and better wettability at the electrode-electrolyte interfaces with low interfacial resistances, the



Rahul Singh is a Ph.D. scholar in the Department of Energy Science and Engineering, IIT Delhi. He received his B. Sc.(Hons) in Physics from Delhi University in 2019. He received M. Sc. degree from Visvesvaraya National Institute of Technology (VNIT), Nagpur, in 2021. He was awarded a prestigious inspire scholarship by the Department of Science and Technology (DST), Government of India. He is awarded inspire fellowship award in 2022. His areas of interest are developing electrolytes for RT Na-S batteries.



Vipin Kumar is an Associate professor in the Indian Institute of Technology Delhi. He received doctorate in materials science and engineering from the School of Materials Science and Engineering at Nanyang Technological University (NTU) Singapore in 2016. He has contributed to various research projects, including electrochemical energy storage using oxide-nanomaterials, miniaturized gas sensor devices based on nanowires and nanosheets assembly, and alkali metal anodes for high-performance batteries. His current research interests lie in electrochemical energy storage using metal-sulfur batteries (e.g., Na-S).

unavoidable dendrite formation and its propagation are roadblocks for ensuring safer and long-term cyclability.^[30] Unlike the solid–electrolyte interphase (SEI) in LEs which passivates the anode but is often mechanically weak and ineffective at suppressing dendrites, the SOLI in SSSBs forms a hybrid layer. This SOLI layer integrates the structural rigidity of the SE with the surface-wetting properties of a minor liquid component. This combination facilitates uniform Na-ion (Na^+) flow, lowers interfacial resistance, and tolerates volume changes during cycling. Consequently, SOLI enhances overall interfacial stability and provides superior dendrite suppression compared to SEI.^[31,32] A schematic representing this is depicted in Figure 1a. In the case of SSSBs, where the conventional organic solvent-based LEs are replaced by employing SSEs, dendrite growth and propagation are restricted. SSEs suppress dendrites through a combination of mechanical rigidity, chemical stability, and controlled ion transport. However, the high interfacial resistance catalyzes nonuniform Na plating/stripping, leading to the formation of a few dendrites (Figure 1b). On the other hand, employing a SOLI through the controlled interfacial reactivity between the Na metal anode and the solid–liquid electrolyte induces spontaneous nucleation and growth of an electrochemically SOLI, which governs subsequent ion transport kinetics.^[33] This hybrid electrolyte consists of both a SE component and a minimal quantity of LE (Figure 1c).

2.1. Ion Transport Facilitation

Even though the SOLI is crucial to the performance of the battery, not much research has been done to fully understand its

implications on the Na anode and the battery performance altogether. This lack of in-depth study has left significant gaps in understanding the underlying causes and direct or indirect effects of the SOLI on the capacity fading and poor cycling stability in SSE. The SOLI provides a pathway for Na ion transport from the electrolyte to the Na anode during the plating and stripping process. Since the SOLI is a combination of inorganic and organic components, the inorganic component of the interphase helps improve the ionic movement across the SOLI. The precise structure and composition of the SOLI influence the migration kinetics of the ions.^[34]

At the Na-SOLI, the mechanism of ion conduction undergoes a notable transition. In the presence of the LE, ion transport primarily occurs through the diffusion of solvated ions, followed by the drift of the ions. However, as the interface shifts toward the SSE, the conduction mechanism changes to a hopping transport mechanism, which is a typical characteristic of SSEs. This shift in ion transport behavior is a critical factor influencing the overall performance of the battery in terms of its electrochemical properties. Here, to understand the SOLI formation, a simple model has been reported to understand the basic thermodynamic aspects of interphase formation in SSSBs.^[35] The change in chemical potential of mobile species (i.e., at solid electrolyte-electrode interphases) develops a driving force for charge redistribution, as the system progresses toward Fermi-level equilibration (see Figure 1d). At the equilibrium, the electrode voltage (vs Na^+/Na) relates to the Na chemical potential (i.e., μ_{Na}) according to the following equation.

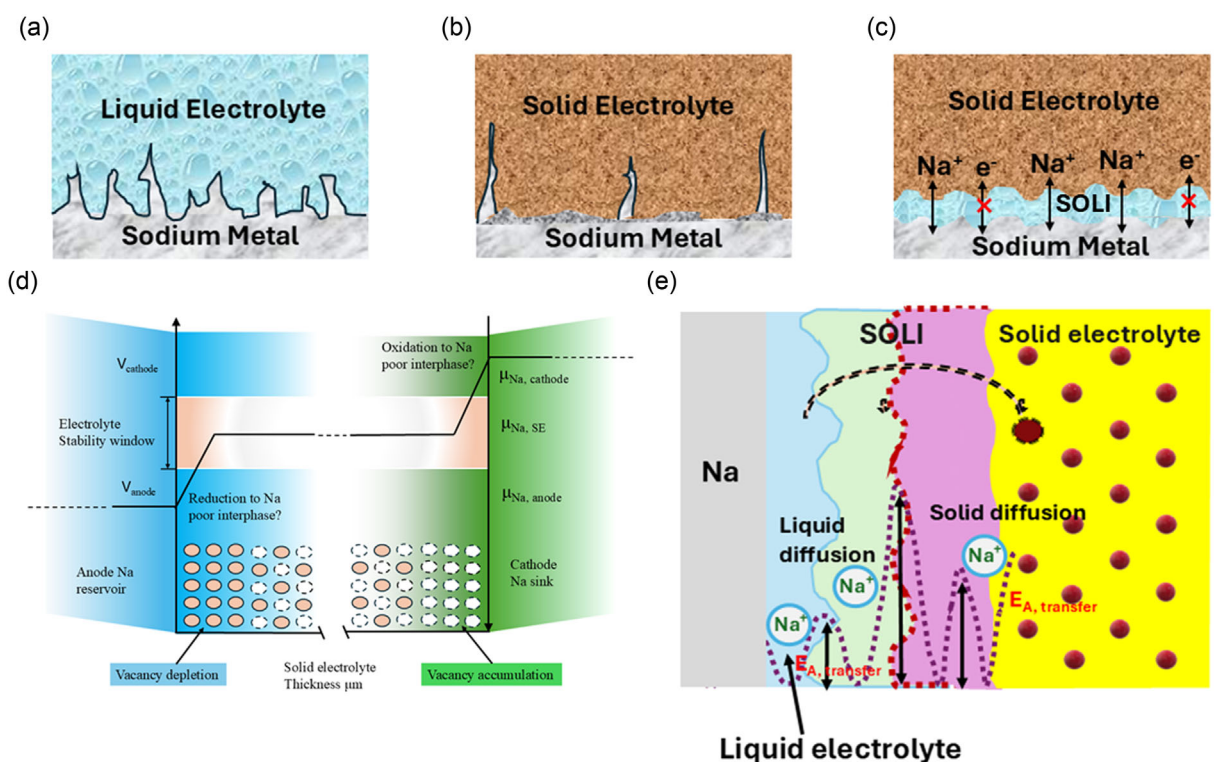


Figure 1. a) Interface formation of Na metal with LE. b) Interface formation of Na metal with SE. c) SOLI formation with Na metal anode. d) Evolution of chemical potential across the SSEs in contact with an anode and a cathode. e) Schematic illustration of the ion transport through the phase boundary between LE and SSE, and formation of the SOLI interface.

$$V = -\mu\text{Na}/F_q \quad (1)$$

where "V" denotes voltage, " μNa " denotes Na chemical potential, "q" represents charge, and "F" is the Faraday constant. Generally, chemical potential drastically changes in the interfacial region due to the rearrangement of the charges. The space-charge layer can be generated at a low potential at the SOLI. The anode induces mobile cations in the electrolyte because metallic Na and SSEs vary in μNa -ion. Mobile cations are driven to the cathode to generate space-charge regions with a high potential. Note that the space-charge areas are referred to as the "electrochemical double layer" at SOLI. This effect may be intensified in all-SSBs because SSEs have more pronounced bulk polarization compared to LEs, owing to their lower permittivity. The reorganization of mobile species in interfacial areas may create distinct concentration gradients, resulting in the reaction (decomposition) of the SSEs with the electrodes, therefore forming a Na-rich interphase at the anode and a Na-poor interphase at the cathode.

2.2. Dendrite Suppression

One of the critical functions of the SOLI is to suppress dendrite growth. Dendrites, unwanted growth of needle-like structures that form during Na deposition, can penetrate through the electrolyte and may compromise the electrolyte properties and eventually lead to an electrical short circuit. The SOLI can regulate Na deposition and help mitigate the formation of dendrites. The inorganic components of the SOLI, in particular, NaF and Na_2S , enhance its mechanical strength, preventing dendrites from piercing through the interphase.^[36]

The SE provides mechanical stability, while the LEs enhance ionic conductivity. The initial interactions between the Na and the electrolyte result in the electrochemical decomposition of the LE, due to the highly negative reduction potential of the Na metal.^[37] The decomposition/reduced products of the LE, that is, the reduced form of the organic and inorganic components, form the SOLI. Concurrently, the SE interacts with the Na surface, contributing to the formation of a multilayer interphase. Figure 1e shows that the two phases' boundaries are present at the interface between the solid and liquid regions. The ion transport through solid phase diffusion, where Na^+ ions migrate through the solid SEI matrix, and liquid phase diffusion occurs if the electrolyte penetrates the SOLI, enabling ion movement in a liquid phase. The SOLI is a complex, multilayered structure of various inorganic and organic species, depending on the electrolyte composition. For example, the liquid component may decompose and form the inorganic components, like NaF, Na_2S , Na_2CO_3 , and NaI, which precipitate onto the Na surface and become part of the SOLI.^[36,38] These inorganic species contribute to the SOLI's mechanical strength and ionic conductivity. On the other hand, the organic components derived from electrolyte solvents or additives may also become a part of the SOLI, necessary for providing flexibility and enhanced transport. The SOLI is crucial for stabilizing the Na anode and improving battery performance.

2.3. Minimizing the Side Reactions

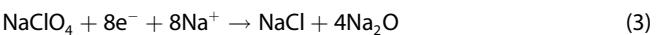
The SOLI acts as a barrier, preventing direct contact between the highly reactive Na metal and the SE. Without this barrier, trace impurities or moisture/oxygen on the surface of the SE may react irreversibly with the Na metal anode, resulting in electrolyte depletion and the formation of unwanted by-products that would degrade the battery's performance. The SOLI stabilizes the surface of the Na metal anode as well as the SE by passivating them and limiting the extent of unwanted side reactions.

2.4. Accommodating Volume Change

A stable SOLI can accommodate the volume fluctuation that occurs during Na deposition and stripping. The inclusion of both solid and liquid components in the electrolyte helps to create a more flexible interphase that can deform and adjust to these changes without losing the integrity of the cell's components. This flexibility prevents the formation of cracks or voids on the SE surface, which could otherwise lead to an increased impedance and cell failure.^[39]

2.5. Reaction Pathways during Initial Formation of SOLI

The formation of SOLI improves interfacial contact, reduces interfacial resistance, and prevents dendrite formation. The preliminary formation includes complex electrochemical and chemical reactions between the Na anode, LE, and SSE. The LE (e.g., organic carbonates or ethers with Na^+ salts) decomposes on the Na metal surface during initial cycling, forming an inorganic/organic hybrid interphase.^[40] Ethylene carbonate (EC) and propylene carbonate (PC) undergo reductive decomposition. The LE infiltrates SSE grain boundaries, reacting with Na-containing SSEs (e.g., $\beta''\text{-Al}_2\text{O}_3$, NASICON, sulfide). The possible reaction pathways are given below.^[41–43]



Here, NaF forms a rigid, dendrite-blocking layer while allowing low-barrier Na^+ diffusion, thus enhancing safety and ionic transport. Na_2S also enhances SE wetting, although it requires electronic insulation to prevent parasitic reactions. Meanwhile, additionally, NaCl and Na_2O contribute to mechanical strengthening and surface passivation but show a tradeoff in ionic conductivity relations. Collectively, these interphase compounds work synergistically to establish stable, low-resistance, and durable interfaces, which are essential for the long-term operation and high-performance of Na SSBs.^[30,35]

2.6. Effect of SOLI on the Electrochemical Performance

SOLI has played a vital role in determining the stable electrochemical performance of all-solid-state sodium metal batteries (ASSMBs). This SOLI layer arises primarily from the electrochemical

reduction of the SE components (sulfide-based, oxide-based, or halide-based) upon contact with the Na metal anode. The initial formation of a thin SOLI layer can enhance interfacial contact by acting as a wetting agent, thereby reducing the initial interfacial resistance and preventing the dendrite formation, which helps facilitate Na^+ ion transfer. However, the SOLI interphase interlayer is not more stable during cycling, and it continuously electrochemically reacts with Na, and the SE starts degrading electrochemical performance. The rapid growth of SOLI increases interfacial impedance over time, manifests as severe voltage polarization, and accelerates capacity fade. Eventually, the uncontrolled formation and instability of the SOLI present a significant bottleneck for attaining high Coulombic efficiency, long cycle life, and safe operation in practical AS-SSMBs, necessitating strategies for its suppression or stabilization. Gao Zhonghui et al.^[44] demonstrated that incorporating TiO_2 into a NZSP SE creates a two-phase composite. This modification significantly enhances key properties, including hardness, grain structure, bulk permittivity, and density. These improvements effectively limit dendrite growth at grain boundaries, microcracks, and micropores. To minimize interfacial resistance and promote uniform Na plating/stripping, the authors used 2 μL of LE (1 M NaClO_4 in EC:DMC) in $\text{Na}/\text{NZSP}(\text{TiO}_2)/\text{Na}$ symmetric cells to remove interfacial resistance. Symmetric cell performance revealed that cells containing the TiO_2 -phase composite exhibited good, stable performance. At a fixed current density of 0.1 mA cm^{-2} , cell shows stable plating/stripping with overpotential of $66 \pm 6 \text{ mV}$ for over 750 h (Figure 2a–c). Furthermore, at different current densities (0.05 to 2 mA cm^{-2}), the $\text{Na}/\text{NZSP}(\text{TiO}_2)/\text{Na}$ cells demonstrated significantly lower overpotential increases compared to cells using unmodified NZSP (Figure 2d,e). Electrochemical impedance spectroscopy (EIS)

analysis of the $\text{Na}/\text{NZSP}(\text{TiO}_2)/\text{Na}$ symmetric cells (Figure 2f) revealed Nyquist plots show two distinct semicircular arcs. Equivalent circuit fitting of this data quantified the interfacial contact resistance (R_e), of $1060 \Omega \text{ cm}^2$ for $\text{Na}/\text{NZSP}/\text{Na}$ and a markedly reduced $149 \Omega \text{ cm}^2$ for $\text{Na}/\text{NZSP}(\text{TiO}_2)/\text{Na}$. Chakraborty et al.^[45] employed Mg^{2+} doping to enhance the electrochemical performance of a NASICON-type SE, synthesizing materials with the general formula $\text{Na}_{3.2+2x}\text{Zr}_{2-x}\text{Mg}_x\text{Si}_{2.2}\text{P}_{0.8}\text{O}_{12}$ (where $0 \leq x \leq 0.228$). To improve interfacial contact in the symmetric cell configuration, a LE consisting of 1 M NaClO_4 in propylene carbonate (PC) was used in $\text{Na}/\text{Mg-NZSP}$ symmetric cell. The symmetric cell was tested with different current density of $25, 50, 75, 100$, and $250 \mu\text{A cm}^{-2}$. Electrochemical characterization was tested in the symmetric cells configuration across a range of current densities ($25, 50, 75, 100$, and $250 \mu\text{A cm}^{-2}$). Notably stable Na plating/stripping behavior was observed. At current densities of $25, 50, 75$, and $100 \mu\text{A cm}^{-2}$, the cells exhibited overpotentials of $+31.6 \text{ mV}$ (charging) / -33.3 mV (discharging), $+72.3 \text{ mV}$ / -73.6 mV , $+108.9 \text{ mV}$ / -112.9 mV , and $+138.1 \text{ mV}$ / -167.9 mV , respectively. These low and symmetric overpotentials reveal uniform Na ion striping and plating.

3. Factors Affecting SOLI Formation

3.1. Pressure

Pressure is a critical parameter in SSBs, influencing mechanical stability, ionic conductivity, interfacial contact, and overall cell performance. Pressure reduces the grain boundary resistance

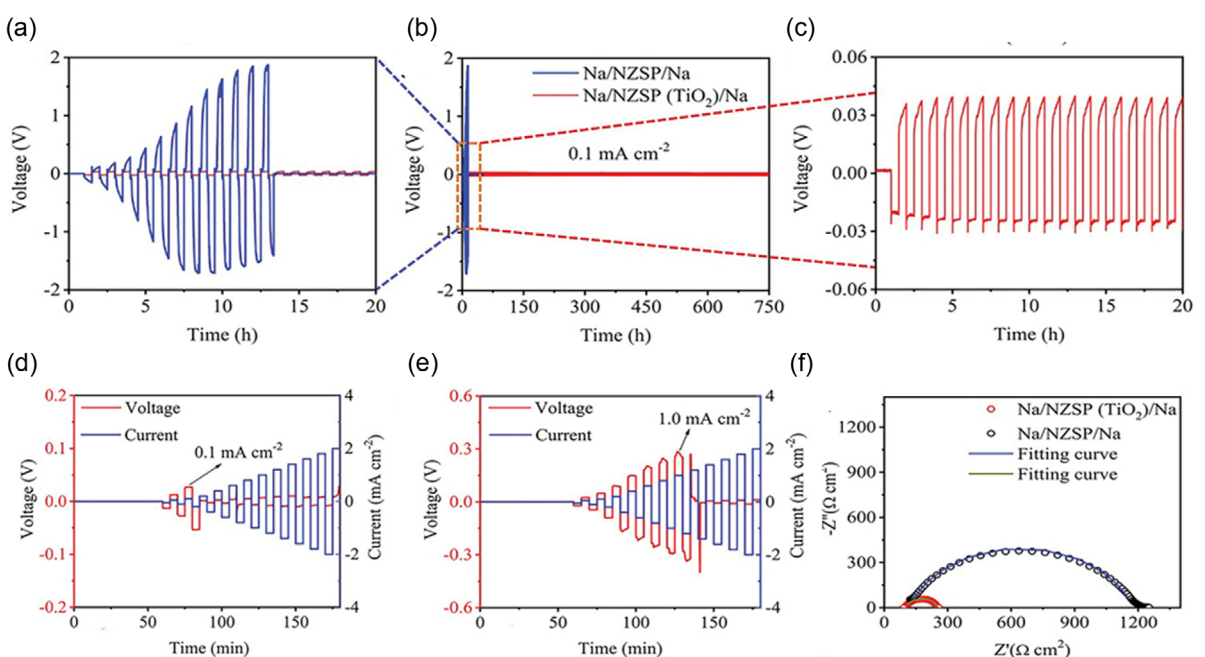


Figure 2. Electrochemical performance of $\text{NZSP}(\text{TiO}_2)$ at room temperature. b) Symmetric cell performance for $\text{Na}/\text{electrolyte}/\text{Na}$ cells at $\pm 0.1 \text{ mA cm}^{-2}$. a,c) Plating/stripping profile. d,e) Measurement of critical current: galvanostatic cycling at current densities ranging from 0.05 to 2 mA cm^{-2} at 25°C for (d) NZSP and (e) $\text{NZSP}(\text{TiO}_2)$. f) Impedance spectra and fits for $\text{Na}/\text{NZSP}/\text{Na}$ and $\text{Na}/\text{NZSP}(\text{TiO}_2)/\text{Na}$ cells. Reproduced with permission.^[44] Copyright 2022, Wiley-VCH.

by minimizing the solid's void gaps, leading to densified material and improved ionic conductivity.^[46] Pressure significantly affects the SOLI formation by improving the contact between the SE and the electrodes, which is crucial for efficient charge transfer. Additionally, excess pressure leads to cracks in SEs, which can lead to short circuits.^[47]

Christian Hänsel et al.^[48] studied the pressure effect on the interfacial contact of Na_3PS_4 alkali metal SSBs. The authors reported that an electrically conductive interface forms when Na_3PS_4 contacts Na metal, which grows rapidly with time during an electrochemical reaction. As a result, the interlayer becomes thick and dense, preventing metallic Na from moving through the Na_3PS_4 pellet and eliminating the chance of a short circuit. Figure 3a shows how cell resistance changes with stack pressure in a symmetric cell configuration, which indicates that cell resistance steadily decreases as stack pressure increases, with increasing stack pressure up to some extent, but after that, the cell resistance does not depend on the pressure.

The authors experimentally found that at stack pressures exceeding 100 MPa, the interfacial resistance decreases due to an increase in contact area at the interface, which reduces the total resistance.^[48] By further increasing the pressure, the interfacial contact area reaches its maximum and cannot expand further. Figure 3b illustrates a continuous increase in open-circuit voltage (OCV) under 45 MPa stack pressure, keeping values exceeding 2 V

during the 240 h test. This shows that there is a significant impedance increase (Figure 3c), from 500Ω at $t = 0 \text{ h}$ to $\approx 20,000 \Omega$ at $t = 240 \text{ h}$, revealing resistive interphase formation and growth at the Na/ Na_3PS_4 interface. Voltage polarization data for Na cells cycled at $50 \mu\text{A}$ ($44 \mu\text{A cm}^{-2}$) to 0.0083 mAh (Figure 3d,e) show a fast increase in overpotential, exhibiting no dependence on stack pressure. By demonstrating the relationship between interfacial degradation and stack pressure in sulfide SSEs, this study provides direction for evaluating approaches to suppress mechanically induced short-circuiting in alkali metal ASSBs, particularly under demanding operational conditions (high currents, capacities) requiring high stack pressures.

The stack pressure is one of the critical parameters to ensure perfect contact of electrode/electrolyte interface. It is worth highlighting that the stack pressure and interface between the electrode/electrolyte is sensitive toward the mechanical properties of the anode. For instance, Uchida et al. reported a low interfacial resistance ($14 \Omega \text{ cm}^2$) for Na/NASICON interface at a high pressure and low current density.^[49] In another contribution, an anode-free solid-state SMBs was designed by depositing a few layers of Na metal over copper electrode coupled under various stack pressure conditions. The findings revealed that Na deposition over copper electrode is more dependent on the extent of current density rather than the stack pressure. These findings are in a sharp contrast with the Li deposition.^[50]

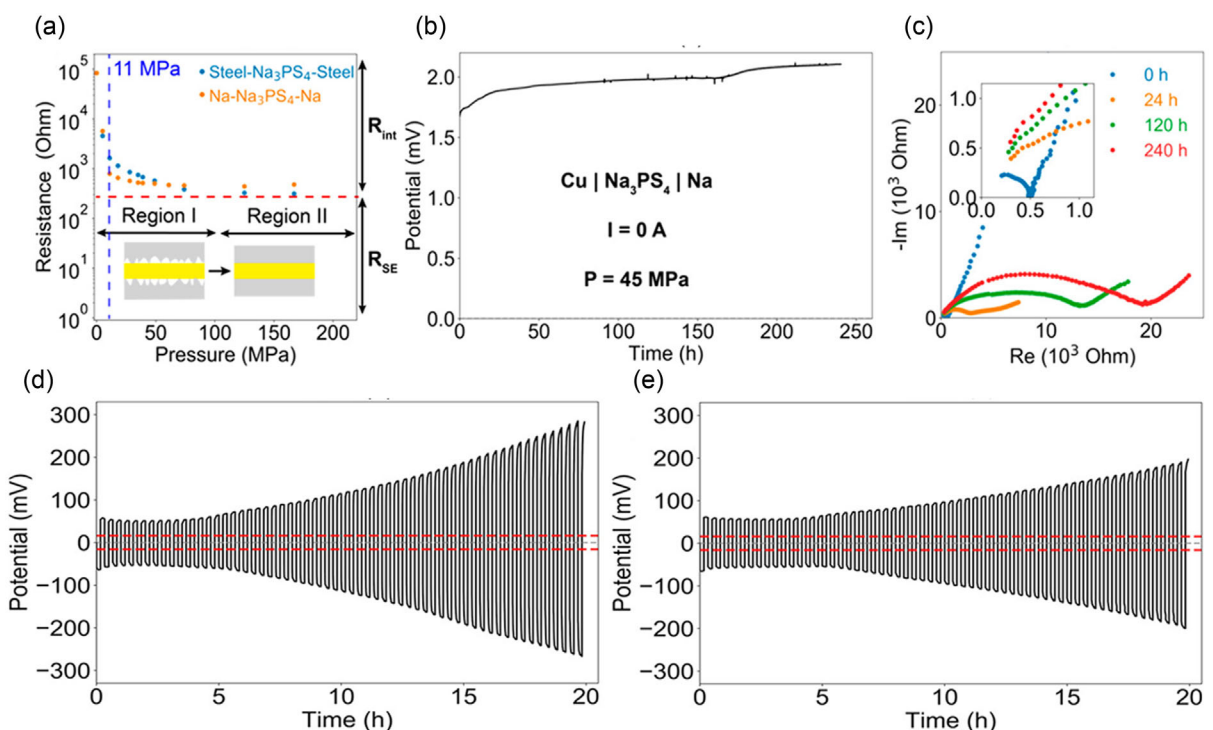


Figure 3. Impact of stack pressure on interfacial resistance and cell stability at zero current and galvanostatic cycling of symmetric cell conditions. a) Na/ Na_3PS_4 /Na cell, indicating that the resistance is dependent on the applied stack pressure. b) OCV variation with time at a constant stack pressure of 45 MPa for the cell Cu/ Na_3PS_4 /Na, c) impedance progression over time for the Cu/ Na_3PS_4 /Na cell under a constant stack pressure of 45 MPa. Results from the galvanostatic cycling of Na/ Na_3PS_4 /Na symmetric cells cycled at $50 \mu\text{A}$ ($0.44 \mu\text{A cm}^{-2}$) for 0.0083 mAh capacity under various stack pressures of d) 5 MPa and e) 11 MPa . Red dotted lines indicate the overpotential calculated from the SE's bulk resistance. Reproduced with permission.^[48] Copyright 2020, American Chemical Society.

3.2. Thickness of Solid-State Electrolytes

The thickness of SSEs critically balances ionic conductivity, energy density, and mechanical stability. In thicker SSE ($>150\text{ }\mu\text{m}$), the chances of dendrite formation are very low, and they also have the capability of stress tolerance but suffer from poor electrode contact. Energy density is also lower due to higher grain boundary resistance. Thinner SSEs ($<150\text{ }\mu\text{m}$) reduce ionic resistance ($R \propto L$), enhancing energy density and enabling faster charging, but there are risks of mechanical defects (e.g., pinholes) and dendrite penetration. **Table 1** summarizes a few critical parameters, including pressure dependency, thickness, interfacial resistance, energy barrier, and ionic conductivity of SSE. A summary and analysis of these innovative ways for interface modification would provide essential direction to the scientific community and commercial uses of SSBs.

3.3. Surface Uniformity

Surface uniformity plays a crucial role in determining battery performance in SSBs. Surface uniformity refers to the homogeneity of the SSE surface in terms of topography, chemical composition, and microstructure. It is essential for determining the quality of the interface between the SSE and the electrodes, which directly affects the battery's performance.^[51] **Figure 4a** shows inhomogeneous interfacial contact between the anode and electrolyte, which creates localized regions of high interfacial resistance at a microscopic level, blocking ion transport and leading to uneven current distribution. Additionally, SSEs show distinct grain boundaries, which act as barriers to Na-ion diffusion and serve as better sites for dendrite nucleation and chemical degradation (Figure 4a). A uniform surface ensures that the LE distributes evenly, reducing localized regions of high resistance. Yongjie Zhao et al.^[52] successfully reduced the interfacial resistance from 90 to $36\text{ }\Omega\text{ cm}^2$ by stabilizing the $\text{Na}/\text{Na}_3\text{Zr}_2\text{Si}_2\text{PO}_{12}$ interface using grain-boundary engineering strategy. An optimized amount of 10 wt\% $\text{Na}_2\text{B}_4\text{O}$ was utilized as the sintering additive to enhance the densification sintering at lower temperatures. Additionally, Qi et al.^[53] studied the effect of polished microstructure of SSE pellets with variation of roughness, contact area, and ravines. An engineered interface of the SSE pellets $\text{Na}_{3.3}\text{Zr}_{1.7}\text{Pr}_{0.3}\text{Si}_2\text{PO}_{12}\text{S}$ showed a very low interfacial resistance of about $11.8\text{ }\Omega\text{ cm}^2$ at room temperature. The findings were credited to polishing the pellets transversely and longitudinally by sandpaper of various mesh sizes (#80, 320, 600, 800, and 1000). Furthermore, Zhendong et al.^[54] successfully reduced interfacial resistance from 813 to $5\text{ }\Omega\text{ cm}^2$ using a uniform and compact SnF_2 film onto the surface of the inorganic SE $\text{Na}_{3.2}\text{Zr}_{1.9}\text{Ca}_{0.1}\text{Si}_2\text{PO}_{12}$ (NCZSP). A conductive layer of Na_xS_n alloys and NaF was observed at the interface because of the *in situ* conversion reaction between molten sodium and SnF_2 , resulting in an improvement in the interfacial contact and suppression of dendritic growth. Zhengyin Yao et al.^[55] recently used N_2 plasma strategy to enhance interfacial stability and ionic conductivity for hybrid solid-state electrolyte (HSE). They have successfully reduced interfacial stability

($26.5\text{ }\Omega\text{ cm}^{-2}$) and achieved high lithium (Li)-ion ionic conductivity of $7.35 \times 10^{-5}\text{ S cm}^{-1}$ at 30°C using these strategies. The crystalline order and glass transition temperature both decrease when SSE is exposed to N_2 plasma. At the same time, this treatment facilitated the spontaneous formation of a highly stable and conductive lithium nitride (Li_3N) layer directly on the HSE surface which reduced structural rigidity and the existence of the Li_3N layer improved lithium-ion (Li^+) mobility across the interface. This led to even more lithium deposition during cycling, thus improving Li^+ transfer kinetics effectively inhibiting the growth of lithium dendrites. Additionally, Dongrong Yang et al.^[56] accomplished enhanced Na-ion diffusion and stable anode interfaces in solid-state Na batteries by an interfacial built-in electric field (IBEF). They oxidized carbon nanotubes (Of@CNT), which were then integrated into HSEs to form a mixed-ion/electron-conducting hybrid solid electrolyte (MIECHSE) (see Figure 4d, e). This field is generated by engineering a laminated hybrid SE incorporating a mixed-conducting layer. The IBEF significantly enhances cycling stability in solid-state symmetric cells up to 26,400 cycles at 0.1 mA cm^{-2} . Furthermore, $\text{Na}/\text{Na}_3\text{V}_2(\text{PO}_4)_3$ (NVP) full cells demonstrated good cycling stability up to 1500 cycles with good capacity retention of 97.4% at 2.0 C . Na/NVP pouch cells also shows a capacity of 65.7 mAh g^{-1} after 50 cycles under 0.19 mA g^{-1} current density.

3.4. Packing Density

The performance of a Na-based SSE is strongly influenced by its packing density. Packing density, which influences many physical and electrochemical characteristics, is the degree of firmly packed together SE particles.^[57] It affects ionic conductivity, electronic conductivity, mechanical stability, interfacial contact, and dendrite suppression. Remarkably, several extrinsic factors influence SSE's practical electronic/ionic conductivities, but packing fraction is the material's intrinsic characteristic that influences practical electronic/ionic conductivities.^[58] Researchers typically refer to structures as close-packed or loose-packed based on how densely the atoms or ions are arranged in the crystal lattice, as shown in Figure 4b,c. There are always tradeoffs between ionic conductivity and electrochemical stability in closed systems and loose pack structures.^[59] The choice between close-packed and loose-packed structures is application-specific.

There are SSEs made of sulfide (Na_3PS_4) and β -alumina that have a closed-packed structure. This structure is very stable mechanically, but it doesn't conduct ions as well. NASICON SSEs offer loose, open framework structures with a packing efficiency of less than 55%, showing high Na ion migration through their channels.^[60] A small amount of LE can fill the gaps in the voids and improve the overall quality of the electrolyte-electrode interface. A tradeoff relation always exists between the SOLI and packing density because the SOLI reduces the overall mechanical strength and chemical stability. The LE needs to be chemically compatible with both the SE and the electrodes to prevent any side reactions. Additionally, the quantity of LEs can introduce safety concerns such as flammability. However, SOLI improves

Table 1. Parametric comparison of various types of SEs.

Solid state electrolyte	Pressure [MPa]	Thickness [μm]	Interfacial resistance [Ω cm²]	Energy barrier [eV]	Ionic conductivity [S cm⁻¹] at 25 °C
$\beta''\text{-Al}_2\text{O}_3$ ^[144]	3.4	1400 ± 30	<10	0.41 ± 0.02	1.6×10^{-3}
$\text{Na}_3\text{Zr}_2\text{Si}_2\text{PO}_{12}$ deposited with graphene ^[145]	12	1800	46	–	5.6×10^{-3}
Ni^{2+} -doped $\text{Na}_{3.4}\text{Zr}_{1.8}\text{Ni}_{0.2}\text{Si}_2\text{PO}_{12}$ ^[100]	–	1000	7.80	0.282	2.284×10^{-3}
NASICON with Sm modification ^[146]	18	–	49	0.24	2.25×10^{-3}
Cubic Na_3PS_4 ^[147]	70	–	–	0.20	4.6×10^{-4}
$\text{Na}_3\text{P}_{0.62}\text{As}_{0.38}\text{S}_4$ ^[148]	400	600–1200	–	0.256	1.46×10^{-3}
$\text{Na}_{3+x}(\text{Sb}_{1-x}\text{Sn}_x)\text{S}_4$ ^[149]	570	–	–	–	–
NZSP with sulfurized polyacrylonitrile layer ^[150]	–	800	200	0.38	–
NZSP with graphene coating layer ^[151]	500	750	46	–	0.6×10^{-3}
Na/TiO_2 -NZSP ^[152]	7	900	101	0.31	–
NZSP welded with Na via ultrasonic welding ^[153]	26	800	22.6	0.291	4.3×10^{-4}
NASICON ^[154]	–	500	11	–	–
$\text{Na}_{3.4}\text{Zr}_2\text{Si}_{2.4}\text{P}_{0.6}\text{O}_{12}$ with $\text{Na-SnO}_2@\text{Na}_{3.4}\text{Zr}_{2.4}\text{P}_{0.6}\text{O}_{12}$ composite anode ^[75]	–	1600	2.4	–	4.1×10^{-3}
Ca^{2+} Doped NASICON ^[155]	–	400	175	–	$>10^{-3}$
$\text{Na}_{3.2}\text{Zr}_{1.9}\text{Ca}_{0.1}\text{Si}_2\text{PO}_{12}$ ^[54]	–	–	5	–	1.46×10^{-3}
Ultrafast sintering of NASICON ^[156]	20	1000	690	0.28	2.62×10^{-4}
Surface potential regulation NZSP ^[157]	–	–	129	0.32	–
Amphiphilic polydopamine (PDA)@NZSP ^[158]	300	1600	–	–	5.90×10^{-4}
Divalent-doped NZSP ^[13]	62	3000–4000	–	0.376	2.7×10^{-3}
$\text{Na}_{3.4}\text{Mg}_{0.1}\text{Zr}_{1.9}\text{Si}_{2.2}\text{P}_{0.8}\text{O}_{12}$ ^[12]	–	–	–	0.285	3.6×10^{-3}
$\text{Na}_{1-x}\text{Zr}_x\text{La}_{1-x}\text{Cl}_4$ ^[159]	260	–	–	0.33	2.9×10^{-4}
$\text{Na}_{3+x+y}\text{Zr}_{2-y}\text{Al}_y\text{Si}_{2+x}\text{P}_{1-x}\text{O}_{12}$ ($0.10 \leq x \leq 0.50$, $0 \leq y \leq 0.1$) ^[160]	0.2	900	–	0.18	6.0×10^{-3}
Na_3BS_3 glass, and $\text{Na}_{2.88}\text{Sb}_{0.88}\text{W}_{0.12}\text{S}_4$ ^[1]	–	2000	–	0.48	125×10^{-3}
Ca^{2+} doped Na_3PS_4 ^[161]	–	–	–	–	–
$\text{Na}_{3.1}\text{Ge}_{0.1}\text{Sb}_{0.9}\text{S}_4$ ^[162]	–	–	–	0.156	5.1×10^{-3}
$\beta''\text{-Al}_2\text{O}_3$ ^[66]	600	1000	65	–	10^{-4}
Ru- doped NZSP ^[163]	598	1200	–	0.24	2.1×10^{-3}
$\text{Na}_{10}\text{SnSb}_2\text{S}_{12}$ ^[92]	180	1500	–	0.23	0.52×10^{-3}
Pr^{3+} -doped NZSP ^[164]	–	1200–1350	–	–	1.27×10^{-3}
Laser etching@NZSP ^[99]	–	–	83	0.268	1.12×10^{-3}
PEOA-PFPE/ Ca-CeO ₂ ^[165]	–	–	–	–	0.89×10^{-4}
NaAlCl_4 ^[166]	–	–	–	–	$\approx 1 \times 10^{-3}$ /30 °C
Ce-substituted NZSP ^[71]	–	–	–	0.33	2.4×10^{-2} /140 °C
Na/NZSP interface ^[52]	–	–	90	0.49	1.72×10^{-3}
F-assisted NZSP ^[167]	120	2000	–	0.33	$1.41 \cdot 10^{-3}$
Self-forming composite NZSP ^[79]	400	1000	–	0.291	4.5×10^{-3}
Cubic Na_3PS_4 ^[168]	360	–	–	0.49	$>10^{-4}$
Na_3SbS_4 via germanium doping ^[162]	480	–	–	0.156	5.1×10^{-3}
Na_3SbS_4 ^[169]	590	–	–	0.20	1.1×10^{-3}
Co-doping@ Na_3SbS_4 ^[170]	–	1600	–	0.193	6.4×10^{-3}
Ca^{2+} -doped NASICON ^[171]	–	–	–	0.346	$\geq 1 \times 10^{-3}$
$\text{Na}_{3-x}\text{SbS}_{4-x}\text{Br}_x$ ^[172]	312	–	–	0.12	0.31×10^{-3}
$\text{Na}_{3-y}\text{PS}_{4-x}\text{Cl}_x$ ^[173]	–	–	80	0.19	1.96×10^{-3}
Mg ²⁺ doped NZSP ^[174]	–	–	93	–	1.5×10^{-3}

Table 1. Continued.

Solid state electrolyte	Pressure [MPa]	Thickness [μm]	Interfacial resistance [Ω cm²]	Energy barrier [eV]	Ionic conductivity [S cm⁻¹] at 25 °C
$\text{Na}_{3+x}\text{Sc}_x\text{Zr}_{2-x}(\text{SiO}_4)_2(\text{PO}_4)$ ^[175]	100	–	–	–	4.0×10^{-3}
SnO _x /Sn Film-NASICON ^[116]	–	–	3	–	5.9×10^{-4}
$\text{Na}_{3-x}\text{Sb}_{1-4x}(\text{SnWCaTi})_x\text{S}_4$ ^[101]	100	1000	–	0.15	6.3×10^{-3}
$\text{ZrO}_2\text{-}2\text{Na}_2\text{ZrCl}_5\text{F}$ ^[140]	–	–	–	0.398	2.1×10^{-5}
$\text{NaM}^{5+}\text{Cl}_6$ ($\text{M}^{5+} = \text{Nb, Ta}$) ^[176]	–	–	–	0.39	–
Na_3YBr_6 ^[177]	300	1000	–	0.15	2.84×10^{-6}
$\text{Na}_{2+x}\text{Zr}_{1-x}\text{MxCl}_6$ ^[178]	–	–	–	0.26	6.5×10^{-6}
$\text{Na}_5\text{SmSi}_4\text{O}_{12}$ ^[179]	300	–	–	0.1	2.9×10^{-3}
NaxBi/NaCl-rich@NZSP ^[39]	–	750	67.6	0.32	4.7×10^{-4}
$\text{NaNbCl}_{6-2x}\text{O}_{x4}$ ^[93]	–	–	–	–	1.03×10^{-4}
$\text{Na}_{3-x}\text{Sb}_{1-4x}(\text{SnWCaTi})_x\text{S}_4$ ^[101]	100	1000	–	0.15	6.3×10^{-3}
IBEF ^{a)} @NSZP ^[56]	–	–	–	–	–

^{a)}IBEF: Interfacial built-in electric field.

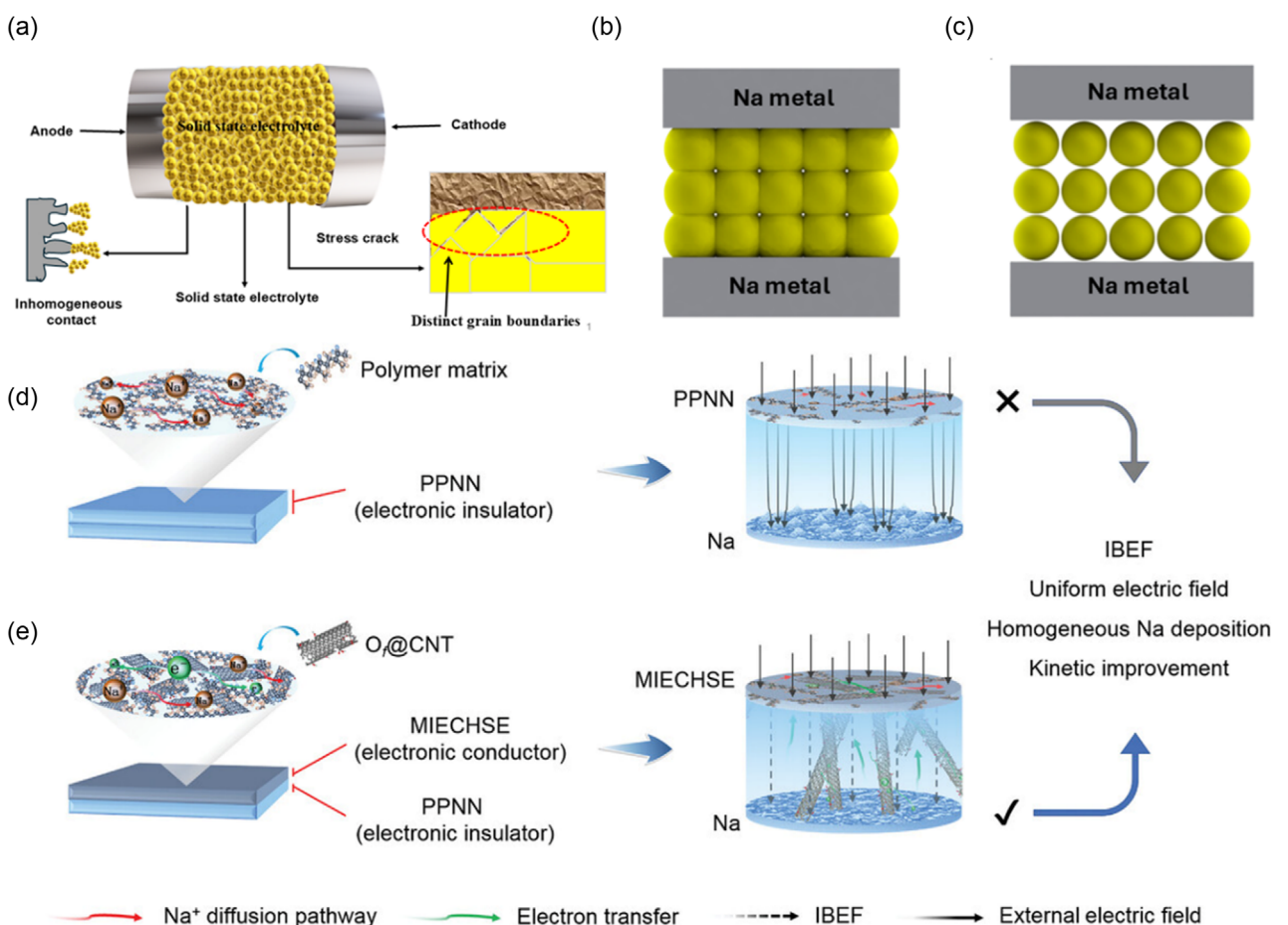


Figure 4. a) Schematic illustration of inhomogeneous contact and the distinct grain boundaries resistance of the SSE. b) Close-packed and c) loose-packed SSE. Schematic of the interfacial electric field. d) The PPNN/Na interface and e) the mixed-ion/electron-conducting hybrid SE/Na interface. Reproduced with permission.^[56] Copyright 2024, Wiley-VCH.

the effective packing at interfaces and grain boundaries, leading to better overall performance.

3.5. Choice of Liquid Electrolytes

The choice of amount and type of LEs in SSBs can significantly affect their performance, including ionic conductivity, interfacial stability, cycle life, and safety. However, the type of LE used can affect the battery's performance. The interface between SSE and an electrode is often imperfect due to surface roughness, voids, and poor adhesion.^[61]

The total resistance (R_{total}) of a SSB can be expressed as

$$R_{\text{total}} = R_{\text{bulk}} + R_{\text{gb}} + R_{\text{effective-interface}} \quad (4)$$

where R_{bulk} = bulk resistance of the SSE, R_{gb} = grain boundary resistance, $R_{\text{interface}}$ = interfacial resistance. Further $R_{\text{effective-interface}}$ defined as

$$R_{\text{effective-interface}} = \frac{(R_{\text{interface}})}{1 + kA} \quad (5)$$

where

κ = wettability factor (depends on the LE's surface tension and viscosity).

A = contact area between the SSE and electrode.

For SSEs, $R_{\text{effective-interface}}$ reduces by using a small amount of LE, which increases the contact area and improves its wettability.

Additionally, the choice of LE affects the ion transport in SSE. Ion transport in solid-state systems occurs through bulk diffusion, grain boundary diffusion, and interfacial diffusion. LEs can enhance ion transport by providing additional pathways for Na^+ migration.

The total ionic conductivity of a hybrid solid–liquid system can be given by the following mathematical equation

$$\sigma = \sigma_{\text{bulk}} + \sigma_{\text{gb}} + \sigma_{\text{effective-interface}} \quad (6)$$

where

σ_{bulk} = bulk conductivity of SSE

σ_{gb} = grain boundary conductivity

$\sigma_{\text{effective-interface}}$ = interfacial conductivity (can be enhanced by a suitable choice of LEs)

The LE helps forming a thin ion-conductive layer on the surface of SSE. The $\sigma_{\text{effective-interface}}$ is given by

$$\sigma_{\text{effective-interface}} = \frac{d_{\text{liquid}}}{d_{\text{interface}}} \sigma_{\text{liquid}} \quad (7)$$

where

σ_{liquid} = ionic conductivity of the LE.

d_{liquid} = thickness of the LE layer.

$d_{\text{interface}}$ = effective interfacial thickness.

For SSE, LEs fill gaps in grain boundaries and provide low-resistance pathways for ionic movements.

The chemistry of the SE must be taken into consideration when choosing a liquid phase. Although oxide ceramics are chemically durable and physically robust, they have high interfacial resistance and poor wetting when used with carbonate or ether LEs. They need low-viscosity carbonate solvents with interfacial coatings to lower resistance.^[62] In order to enhance Na-ion conductivity and interfacial contact with Na metal, Liu et al.^[63] synthesized a number of NASICON-type materials ($\text{Na}_{3+x}\text{Zr}_{2-x}\text{Sc}_x\text{Si}_2\text{PO}_{12}$) with certain compositions. Their research demonstrated that adjusting the Sc content decreased interfacial resistance and increased bulk ionic conductivity, underscoring the significance of chemical compatibility between the contacting phase and the oxide electrolyte surface. This study shows that compositional control can modulate interfacial properties even in systems with a solid phase predominance. It also shows that careful electrolyte–interface engineering is necessary to lower interfacial resistance and permit stable cycling with metallic Na. Sulfide-based electrolytes provide for good physical contact by combining considerable mechanical softness with near-liquid ionic conductivity ($\approx 10^{-2} \text{ S cm}^{-1}$). Na_3PS_4 and Na_3SbS_4 are common examples, providing high ionic conductivity ($\approx 10^{-4} \text{--} 10^{-3} \text{ S cm}^{-1}$). Nevertheless, they decompose interfacially with Na metal to generate layers such as Na_2S , Na_3P , or Na_3Sb , which causes an increase in impedance. These sulfide-based electrolytes can chemically react with common liquids and are sensitive to moisture; therefore, they prefer inert, nonaqueous solvents that minimize side reactions, including low-polarity ethers, formulated with chemicals to preserve compatibility and inhibit the production of H_2S .^[64] In addition to forming gel polymer electrolytes (GPEs) using carbonate or ether solvents, polymeric electrolytes naturally permit droplet-like wetting. GPEs combine strong ionic conductivity ($> 10^{-3} \text{ S/cm}$) and mechanical toughness using solvents such as carbonate- or ether-based liquids. Polymer–salt interactions determine the solvent selection, for example, dimethoxyethane for PEO and PC for PVDF-HFP gels.^[65] Kim et al. and authors showed how adding only a small amount of LE (1 M NaSO_3CF_3 in TEGDME, approximately 15 wt%) to a solid-state system that uses NASICON-type particles scattered throughout a PVDF-HFP polymer matrix greatly improves battery performance. The SSE and LE's chemical compatibility is crucial to this enhancement. Because of this compatibility, the liquid may efficiently moisten the NASICON particles' surface, filling in gaps and separating grains. This lowers interfacial resistance, which normally restricts ion transport in solid-state systems. The LE's presence improves overall ionic conductivity by facilitating the growth of continuous Na-ion channels between the ceramic particles. The polymer matrix in the hybrid electrolyte also gives it mechanical flexibility, which, when paired with stable interfacial chemistry, inhibits the development of resistive interphases and prolongs electrochemical stability.^[63] Table 2 shows the choice of the LE with respect to the SE.

The solid–liquid compatibility depends on several electrochemical and mechanical systems. For oxide-based (NASICON, β -Alumina) SSE, organic carbonate-based electrolytes such as 1 M NaClO_4 in ethylene carbonate: dimethyl carbonate (EC:

Table 2. Choice of the liquid electrolyte with respect to the SE.

SSE	Salt	Solvent
$\text{Na}_{3+x}\text{Zr}_{2-x}\text{Sc}_x\text{Si}_2\text{PO}_{12}$ ^[180]	NaSO_3CF_3	TEGDME
$\beta''-\text{Al}_2\text{O}_3$ ^[66]	NaClO_4	EC/DMC (1:1) + 5% FEC
NASICON ^[156]	NaPF_6 in EC: DEC = 1:1	EC/DEC = 1:1

DMC) are used because these electrolytes show good electrochemical stability up to ≈ 4.5 V versus Na/Na⁺ and are compatible with oxide-based SSEs due to their low reactivity with oxide-based systems.^[66–68] In some cases, researchers also used ionic liquids (NaTFSI, NaFSI, NaPF₆, NaBF₄, NaN(CN)₂) electrolytes for higher ionic conductivity and wider electrochemical stability.^[67] Organic carbonates (1 M NaPF₆ in EC: DEC) are also used for sulfide-based SSE because these electrolytes are less reactive with a sulfide-based system.^[67] GPEs (like PEO-NaTFSI) mixed with LEs have also been used with SSE to make the interface more stable. The parametric analysis of various types of SSE is given in Table 3.

4. Challenges of Na Metal Anode in All-Solid-State Batteries

Apart from the high reactivity of Na metal anode, which leads to unstable interfaces, it also suffers from non-uniform deposition that cause internal short circuits.^[69] This limits the cycling stability, especially when paired with SSEs. Moreover, Na metal anode problems, such as structural alterations, resistive interfacial contact, and volume change, are common in batteries that use SSEs.

4.1. Structural Change

The deposition of sodium metal poses considerable difficulties in SSBs, especially those employing inorganic SSEs. The volumetric variations of Na metal over successive charging and discharging cycles hinder the preservation of a stable interface between the Na metal and the SSE.^[70] The rigid nature of inorganic SSEs and the need for high operational pressures can lead to poor contact and interface degradation.^[71] This deterioration increases the polarization resistance of the cell, ultimately affecting its performance. Xianjian et al.^[33] demonstrated interfacial engineering strategies for Na metal anodes in ASSBs. Na high reactivity inherently triggers side reactions with rigid SSEs, as illustrated in Figure 5a. Additionally, Figure 5b reveals that poor interfacial contact between Na and SSEs causes uneven ion transport and raised the impedance. Studies further show that stress produced by Na anode volume changes during plating/stripping (Figure 5c) restricts ion transport. This interfacial stress may crack SSEs, eventually resulting in battery failure over long cycling. Haoyu Fu et al.^[72] achieved a significant reduction in Na/NASICON interfacial resistance, decreasing from 1658 to 101 $\Omega \text{ cm}^2$. They formed Na-SiO₂ composite, which reduces the surface stiffness of Na metal. Cross-sectional SEM imaging reveals a distinct interfacial gap between pristine Na metal and NASICON

(Figure 5d), revealing poor physical contact. In contrast, the Na-SiO₂ composite was drop-cast directly onto the NASICON SE (Figure 5e), resulting in dramatically reduced interfacial resistance. Additionally, Yifan Gu et al.^[39] engineered a flexible BiCl₃/polytetrafluoroethylene (PTFE) interlayer between a NZSP SE and a Na metal anode. During cycling, BiCl₃ reacts with Na to in situ form a multifunctional NaxBi/NaCl-rich interfacial layer. This flexible structure significantly enhances interfacial contact, suppresses void formation, and reduces interfacial resistance. Consequently, symmetric Na/BiCl₃@NZSP/Na cells exhibit a significant decrease in interfacial resistance (from 1252.1 to 67.6 Ω) and a substantial critical current density of 2 mA cm^{-2} at 25 °C, as illustrated in the Figure 5f. Cross-sectional SEM and EDS mapping of the pristine Na/NZSP interface shows distinct gaps (Figure 5g–l), which contribute to high interfacial resistance and poor cycling stability. In contrast, the Na/BiCl₃@NZSP interface maintains good contact with NZSP, as confirmed by cross-sectional SEM and EDS analysis (Figure 5i–n). Dongchen et al.^[73] achieved a reduced interfacial resistance of 23 $\Omega \text{ cm}^2$ by employing a Na-Au alloy interlayer. The Na–Au alloy interlayer reduces the generation of the Na₂SiO₃ byproduct, improves Na⁺ transport, and promotes uniform Na plating and stripping. Additionally, Jin et al.^[74] developed a Na₁₅Sn composite anode through physical mixing with a Na superionic conductor. The interfacial resistance decreased to 6.5–10.5 $\Omega \text{ cm}^2$ without subjecting to significant mechanical compression. The incorporation of Na₁₅Sn₄ within the Na matrix facilitates the diffusion of Na⁺ ions in the composite anode, thus enhancing diffusion kinetics. Keshuang et al.^[75] engineered a hybrid Na anode to mitigate cycle induced interfacial resistance. To reduce the interface deterioration, the authors integrated SE particles into the molten Na metal.

4.2. Poor Interfacial Stability

When employing SSSBs and shielded electrodes, the SEs' interfacial stability at the electrodes is essential. It has a major effect on the cell's efficiency as well as the rate of charge transfer at the interface, which affects the SE resistance overall.^[71] Fupeng Li et al.^[76] reported in order to examine the formation and behavior of these interfaces, and they developed numerous computational and experimental methods. The SE layer is positioned between compressed powder electrode layers (positive and negative electrodes) in order to create bulk-type all-SSSBs, where the electrode layers are composed of SEs (like Na₃PS₄) and active materials (like Na metal). Consequently, electrons move from active material to collectors via conductive additive conduction pathways (acetylene black in electrode layers) while Na ions move across the interface from active material to SE. All-SSSBs are classed as inorganic solid-electrolyte and organic solid-electrolyte batteries based on the numerous SEs outlined above.^[77,78] For example, when the Na₃PS₄ electrolyte interacts with Na metal, it decomposes into a poorly ion-conductive and electronically insulating layer composed of Na sulfide and Na phosphide.^[79] The particle size distribution within SSEs is a key parameter for determining their internal microstructure and the formation of effective

Table 3. Parametric analysis of different types of SE with and without SOLI interphase.

Electrolyte	Prototype	Ionic conductivity [S cm ⁻¹], operating temperature	Performance in full SSMBs	SOLI required
Oxide based	$\beta''\text{-Al}_2\text{O}_3^{[66]}$	–	Initial discharge capacity of 95.4 mAh g ⁻¹ at 0.5C in NVP// $\beta''\text{-Al}_2\text{O}_3/\text{UW-Na}^a$	10 µL of LE 1 M NaClO ₄ in EC/DMC (1:1) + 5% FEC
	$\beta''\text{-Al}_2\text{O}_3^{[181]}$	–	Initial discharge capacity 87.9 mAh g ⁻¹ at 0.1C in NVP//SC-treated $\beta''\text{-Al}_2\text{O}_3/\text{Na}$	10 µL of LE 1 M NaClO ₄ in EC/DMC (1:1) + 10% FEC
	Y_2O_3 (0.5 wt%) ^[182]	3.48×10^{-2} /300 °C	–	–
	MgO (0.4 wt%) ^[183]	0.137/300 °C	–	–
	TiO ₂ (2 wt%) and ZrO ₂ (10 wt%) ^[184]	5.4×10^{-6} /25 °C	–	–
	Ultrafast sintering of NASICON ^[156]	2.62×10^{-4} /25 °C	Initial discharge capacity is 102 mAh g ⁻¹ at 0.2C in Na//NASICON//NVP	5 µl LE (with NaPF ₆ in EC: DEC = 1:1 by volume)
	$\text{Na}_{3.125}\text{Zr}_{1.75}\text{Sc}_{0.125}\text{Ge}_{0.125}\text{Si}_2\text{PO}_{12}^{[185]}$	4.64×10^{-3} /25 °C	Discharge Capacity 101 mAh g ⁻¹ (0.2 C) in NVP half-cells	Few drops of 1 M NaPF ₆ in EC/DMC + 10% FEC added on both sides of the pellet
	Ru-doped NZSP ^[163]	8.1×10^{-4} /25 °C	Initial discharge capacity 87 mAh g ⁻¹ at 0.3C in NVP//Ru-NZSP//Na	2 µl LE of 1 M NaClO ₄ in EC: DMC
	Ni ²⁺ -doped $\text{Na}_{3.4}\text{Zr}_{1.8}\text{Ni}_{0.2}\text{Si}_2\text{PO}_{12}^{[100]}$	2.284×10^{-3}	–	1 M NaClO ₄ in EC:PC (1:1) + 5% FEC
	Laser etching@NZSP ^[99]	1.12×10^{-3}	Initial discharge capacity 116.0 mAh g ⁻¹ at a 1 C rate in NVPF half-cell	1 M NaClO ₄ in EC:PC (1:1) with 5% FEC
Oxygen regulated Na: NASICON ^[119]		–	Initial discharge capacity 111.1 mAh g ⁻¹ at 0.5C in ORNa/NZSP//NVP	5 µl carbonate based LE
SnO _x /Sn Film- NASICON ^[116]		5.9×10^{-4} /25 °C	Initial discharge capacity 123.1 mAh g ⁻¹ , at 0.2C in NTP//SnO _x /Sn-NZSP//Na	5 µL of 1 mol L ⁻¹ NaClO ₄ in EC: DMC
Ca ²⁺ -doped NASICON ^[155]		10^{-3} /25 °C	Initial discharge capacity 103.1 mAh g ⁻¹ , at 0.2C in NVP//NZSP//Na	4 µL polymer electrolyte
$\text{Na}_{3.4}\text{Zr}_{2}\text{Si}_{2.4}\text{P}_{0.6}\text{O}_{12}$ with $\text{Na-SnO}_2@\text{Na}_{3.4}\text{Zr}_{2}\text{Si}_{2.4}\text{P}_{0.6}\text{O}_{12}$ composite anode ^[75]		4.1×10^{-3} /25 °C	Initial discharge capacity is 110.7 mAh g ⁻¹ at 5C in NVP//NZSP//h-Na	Small amount of 1 M NaPF ₆ in EC/DEC/PC (4:4:2, volume ratio)
NZSP with surface impurity removed ^[154]		–	Initial discharge capacity of 106 mAh g ⁻¹ at 1C	1 M NaClO ₄ in EC: DEC = 1:1 vol% with 2% FEC addition
NZSP welded with Na via ultrasonic welding ^[153]		4.3×10^{-4} /25 °C	Initial discharge capacity of 110 mAh g ⁻¹ at 0.1 mA cm ⁻² in UW-Na// $\text{Na}_3\text{Zr}_2\text{Si}_2\text{PO}_{12}$ //NVP	1 M NaClO ₄ in EC/DMC (1:1) + 5% FEC
NZSP with BiO _x coating layer ^[186]		–	Second discharge capacity of 99.3 mA h g ⁻¹ at 1C in NVP(LE)//NZSP//Na-BiO _x	5 µL LE (1 M NaClO ₄ in EC/DMC (1:1) + 5% FEC)
NZSP with TiO ₂ coating layer ^[152]		–	Delivers a capacity of 106.3 mA h g ⁻¹ at 0.1C in NVP//NZSP- TiO ₂ //Na	10 µL LE of 1.0 M NaClO ₄ in PC + 5.0% FEC
$\text{Na}_3\text{Hf}_2\text{Si}_2\text{PO}_{12}$ with Pb coating layer ^[187]		1.48×10^{-3} /25 °C	Initial discharge capacity of 107.9 mAh g ⁻¹ at 1C in Na/Pb- $\text{Na}_3\text{Hf}_2\text{Si}_2\text{PO}_{12}$ -Pb//Na	Tiny amount of the LE
NZSP with AlF ₃ coating layer ^[188]		–	Initial discharge capacity of 111.0 mAh g ⁻¹ at 0.1 mA cm ⁻² in NVP//NASICON//Na	10 µL LE of 1.0 M NaClO ₄ in PC with 5.0% FEC
NZSP with graphene coating layer ^[151]		–	Initial capacity of 108 mAh g ⁻¹ at 1C in NVP//LE/G-NASICON//Na	Small amount of LE
NZSP with sulfurized polyacrylonitrile layer ^[150]		–	Initial capacity of 114.1 mAh g ⁻¹ at 0.5C in NVP//SPAN-NASICON//Na	10 µL LE of 1.0 M NaClO ₄ in PC with 5.0% FEC
$\text{Na}_{3.3}\text{Zr}_{1.7}\text{La}_{0.3}\text{Si}_2\text{PO}_{12}^{[189]}$		3.4×10^{-3} /25 °C	Initial capacity of 113 mAh g ⁻¹ , CE of 97.5% in NVP//Na cells.	–
F-assisted NZSP ^[167]		1.41×10^{-3} /25 °C	Initial capacity of 85.9 mAh g ⁻¹ (0.5 C) in NVP//Na cells.	10 µL LE (1 M NaClO ₄ in propylene carbonate)
NZSP ^[157]		8.5×10^{-4} /25 °C	Initial capacity of 103 mAh g ⁻¹ (0.1 A g ⁻¹) in $\text{Na}_3\text{V}_{1.5}\text{Cr}_{0.5}(\text{PO}_4)_3$ //Na cells.	Few drops of NaClO ₄ in a solvent

Table 3. Continued.

Electrolyte	Prototype	Ionic conductivity [S cm ⁻¹], operating temperature	Performance in full SSMBs	SOLI required
	$\text{Na}_3\text{Zr}_{1.9}\text{Ce}_{0.1}\text{Si}_2\text{PO}_{12}$ ^[14]	$2.20 \times 10^{-3}/25^\circ\text{C}$	Initial capacity 87 mAh g ⁻¹ (0.3C) in NVP//NZSPR8//Na	1 A ^μ l of 1 M NaClO ₄ solution in EC/DMC at cathode side
	Pr ³⁺ doped NZSP ^[164]	$0.9 \times 10^{-3}/25^\circ\text{C}$	Initial capacity 109.1 mAh g ⁻¹ (0.5C) in $\text{Na}_3\text{V}_2(\text{PO}_4)_3/\text{C}/\text{Na}_{3.3}\text{Zr}_{1.7}\text{Pr}_{0.3}\text{Si}_2\text{PO}_{12} // \text{Na}$	10 μL of LE (1 M NaClO ₄ in EC/DMC (1:1) + 5% FEC)
	$\text{Na}_{3+x}\text{Zr}_{2-x}\text{Sm}_{0.2}\text{Si}_2\text{PO}_{12}$ (0 ≤ x ≤ 0.4) ^[146]	$2.25 \times 10^{-3}/25^\circ\text{C}$	–	0.4 mL ionic liquid (saturated NaTFSI in Py13FSI)
	$\text{Na}_{3.4}\text{Mg}_{0.1}\text{Zr}_{1.9}\text{Si}_{2.2}\text{P}_{0.8}\text{O}_{12}$ ^[12]	$3.6 \times 10^{-3}/25^\circ\text{C}$	Initial capacity of 93.3 mAh g ⁻¹ (0.1 C) in NVP//Na cells.	–
	NZSP-10 wt% $\text{Na}_2\text{B}_4\text{O}_7$ ^[52]	$1.72 \times 10^{-3}/25^\circ\text{C}$	Initial capacity of 80 mAh g ⁻¹ (0.1 A g ⁻¹) in $\text{Na}_3\text{V}_{1.5}\text{Cr}_{0.5}(\text{PO}_4)_3/\text{Na}$ cells.	–
	$\text{Na}_{3.4}\text{Zr}_{1.9}\text{Ti}_{0.1}\text{Si}_2\text{PO}_{12}$ ^[190]	$4.72 \times 10^{-4}/25^\circ\text{C}$	–	–
	$\text{MAICl}_{4-2x}\text{O}_x$ (MACO, M = Li, Na, 0.5 < x) ^[166]	$1.0 \times 10^{-3}/30^\circ\text{C}$	–	–
Sulfide and solid Polymer based	$\text{Na}_3\text{P}_{0.62}\text{As}_{0.38}\text{S}_4$ ^[191]	$1.46 \times 10^{-3}/25^\circ\text{C}$	Initial capacity of 118 mAh g ⁻¹ in TiS ₂ //Na-Sn cells.	–
	c-Na ₃ SbS ₄ ^[191]	$2.8 \times 10^{-3}/25^\circ\text{C}$	Initial capacity 360 mAh g ⁻¹ in S//Na ₃ SbS ₄ //PETEA-Na full cell	NaClO ₄ /tetraglyme-based LE
	Na ₃ SbS ₄ ^[169]	1.1×10^{-3}	Initial capacity of 108 mAh g ⁻¹ (50 μAcm ⁻²) in NaCrO ₂ //Na cells	–
	$\text{Na}_{3-x}\text{SbS}_{4-x}\text{Br}_x$ ^[172]	3.1×10^{-4}	Initial capacity of 110 mAh g ⁻¹ (0.1 C) in TiS ₂ //Na ₁₅ Sn ₄ cells	–
	$\text{Na}_{3.02}(\text{Sb}_{0.98}\text{Sn}_{0.02})\text{S}_4$ ^[149]	$2 \times 10^{-4}/25^\circ\text{C}$	–	–
	$\text{Na}_{10}\text{GeP}_2\text{S}_{12}$ ^[96]	$4.7 \times 10^{-3}/25^\circ\text{C}$	–	–
	Na ₃ PS ₄ ^[147]	4.6×10^{-4}	Initial capacity of 130 mAh g ⁻¹ (0.013 mA g ⁻¹) in Na ₁₅ Sn ₄ //Na ₃ PS ₄ //NaCrO ₂	–
	$\text{Na}_{3-y}\text{PS}_{4-x}\text{Cl}_x$ ^[173]	$1.96 \times 10^{-4}/25^\circ\text{C}$	–	–
	$\text{Na}_{2.73}\text{Ca}_{0.135}\text{PS}_4$ ^[173]	9.4×10^{-4}	Initial capacity of 198 mA h g ⁻¹ (0.06 C) TiS ₂ //Na _{2.73} Ca _{0.135} PS ₄ //Na-Sn	–
	$\text{Na}_{3.1}\text{Ge}_{0.1}\text{Sb}_{0.9}\text{S}_4$ ^[162]	5.1×10^{-3}	–	–
Hybrid polymer solid SSEs with NaClO ₄ (POSS-4PEG2K(NaE16)) ^[195]	$\text{Na}_{10}\text{SnP}_2\text{S}_{12}$ ^[192]	$4 \times 10^{-4}/25^\circ\text{C}$	–	–
	Na ₃ PSe ₄ ^[193]	$1.16 \times 10^{-3}/25^\circ\text{C}$	–	–
	$\text{Na}_{2.88}\text{Sb}_{0.88}\text{W}_{0.12}\text{S}_4$ ^[1]	$125 \times 10^{-3}/60^\circ\text{C}$	Initial capacity of 160 mAh g ⁻¹ (0.13 mA g ⁻¹) in Na ₁₅ Sn ₄ -KB//Na ₃ BS ₃ //Na _{2.88} Sb _{0.88} W _{0.12} S ₄ //TiS ₂	–
	Na[(FSO ₂)(n-C ₄ F ₉ SO ₂)N/PEO ^[194]	$3.36 \times 10^{-4}/80^\circ\text{C}$	Initial capacity of 122.4 mAh g ⁻¹ (12 mA g ⁻¹), capacity retention is 70% after 150 cycles (120 mA g ⁻¹) in Cu _{1/9} Ni _{2/9} Fe _{1/3} Mn _{1/3} O ₂ /Na cells	–
	Poly(trimethylene carbonate)/NaFSI(PTMC:NaFSI) ^[96]	5×10^{-5}	Initial capacity of 90 mAh g ⁻¹ (0.5 C) in Prussian blue/Na cells	–
Solid polymer SSEs based on star-like hyperbranched D6FD;-cyclodextrin ^[97]		$1.3 \times 10^{-4}/60^\circ\text{C}$	102.4 mAh g ⁻¹ , capacity retention of 87.8% after 80 cycles (0.1 C) in NaNi _{1/3} Fe _{1/3} Mn _{1/3} O ₂ /Na cells.	–

^aUW, ultrasound welding; NZSP, $\text{Na}_3\text{Zr}_2\text{Si}_2\text{PO}_{12}$; NVP, $\text{Na}_3\text{V}_2(\text{PO}_4)_3$; ORNa, oxygen regulated Na; NTP, $\text{NaTi}_2(\text{PO}_4)_3$.

interfaces in SSBs.^[80] While larger particles help void formation and fracture, reducing density and ionic conductivity, smaller particles increase grain boundary density, compromising mechanical stability and equally impeding ionic conduction (shown in

Figure 6a,b).^[80,81] Additionally, Pu Hu et al.^[82] reported the interface between Na metal anode and sulfide-based SSE in a symmetric cell configuration (see Figure 6c), which shows the cell opened inside the glove box after 160 h. An unstable contact between Na

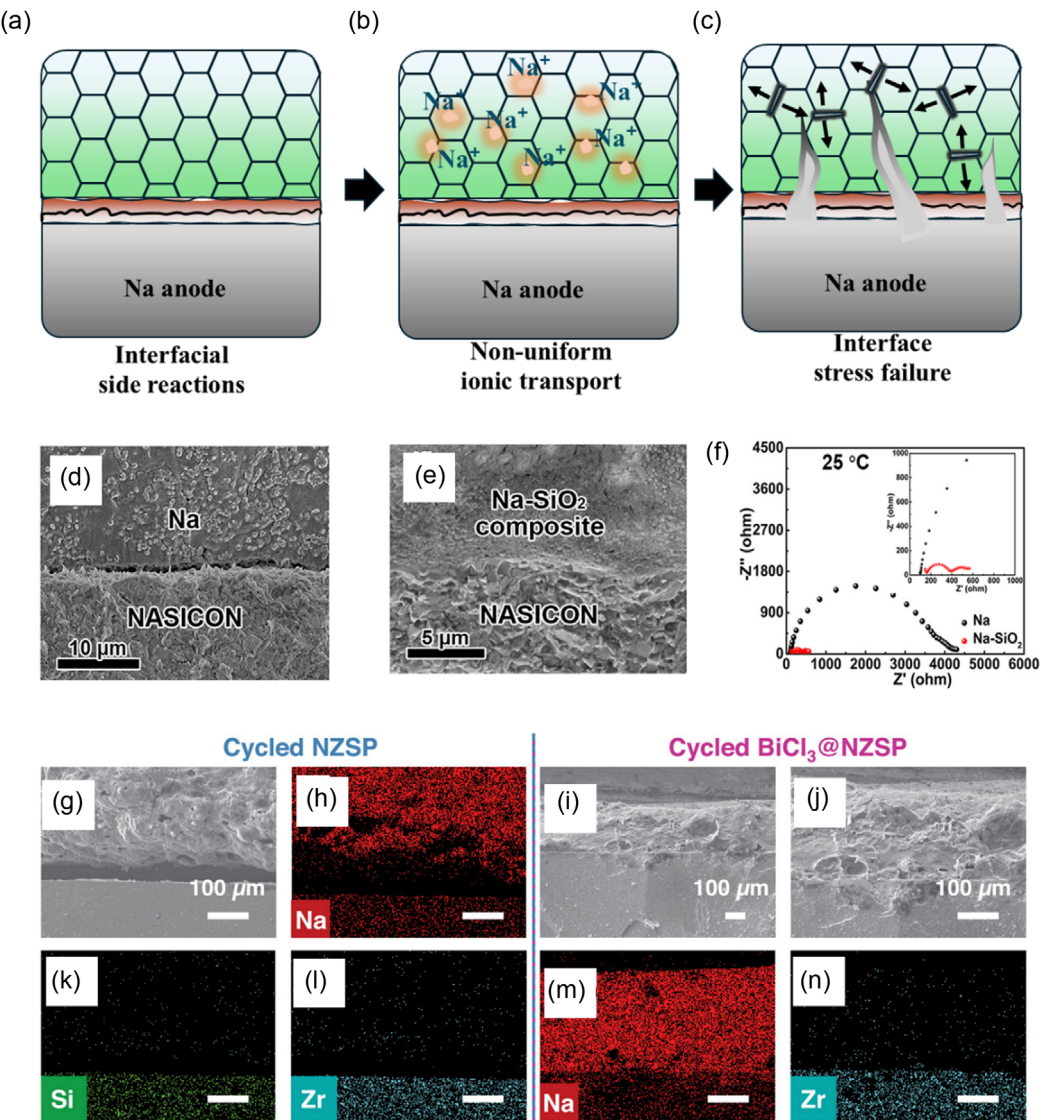


Figure 5. a) Schematics indicating possible reactions at Na metal-SSE interface; b) nonuniform ion transport due to poor wettability; c) cell failure due to interfacial stress. SEM images showing the cross-section of the d) NASICON/Na and e) NASICON/Na-SiO₂ interfaces. f) EIS profiles for symmetric ASSBs utilizing a pristine Na/NZSP anode and Na/BiCl₃@NZSP. Reproduced with permission.^[72] Copyright 2020, American Chemical Society. g) Cross-sectional SEM and h,k,l) corresponding EDS mapping images of Na/NZSP after 50 cycles at 0.1 mA cm⁻²/0.1 mAh cm⁻². i,j) Cross-sectional SEM of Na/BiCl₃@NZSP and m,n) corresponding EDS mapping images of Na/BiCl₃@NZSP after 50 cycles at 0.1 mA cm⁻²/0.1 mAh cm⁻². Reproduced with permission.^[39] Copyright 2024, Wiley-VCH.

and Na₃SbS₄ was shown by the scuffed electrolyte surface with visible black patches. As seen in Figure 6d, the overpotential of the cell grew consistently with cycling time as a result of the constant Na deposition throughout cycling. Figure 6e displays the symmetric cell's EIS spectra both before and after cycling. There is no significant change in the bulk resistance of the cell after cycling (from 87.2 to 90.9 Ω). However, there is a significant change in the interfacial resistance before and after cycling, increasing from 318.2 to 6,475.0 Ω. Additionally, the resistance for charge transfer has risen from 13.6 to 464.3 Ω. Figure 6f shows that there are also increases in specific area resistance (ASR) from the initial 25 h from 750 to 1,860 Ω cm².

Volume fluctuations during Na metal plating and stripping also affect the Na metal/SSE interface. Better contact between the sodium metal anode and the SSE, which is distinguished

by strong ionic conductivity, chemical inertness, and electrochemical stability, must be established and maintained. This close interfacial contact reduces interfacial impedance, generally measured using area-specific resistance (ASR).^[83] This intimate contact also promotes uniform stripping and plating of Na ions. The ASR of the interface between Na metal and the SSE can be calculated using the following relation.

$$\text{ASR} = R_{\text{inter}} \times S \quad (8)$$

where S represents the effective contact area between Na and SSE, and R_{inter} denotes the interfacial resistance obtained from the cell's internal resistance. When both sides' contact areas are engaged, as in symmetric cells using Na metal as electrodes, the measured R_{inter}

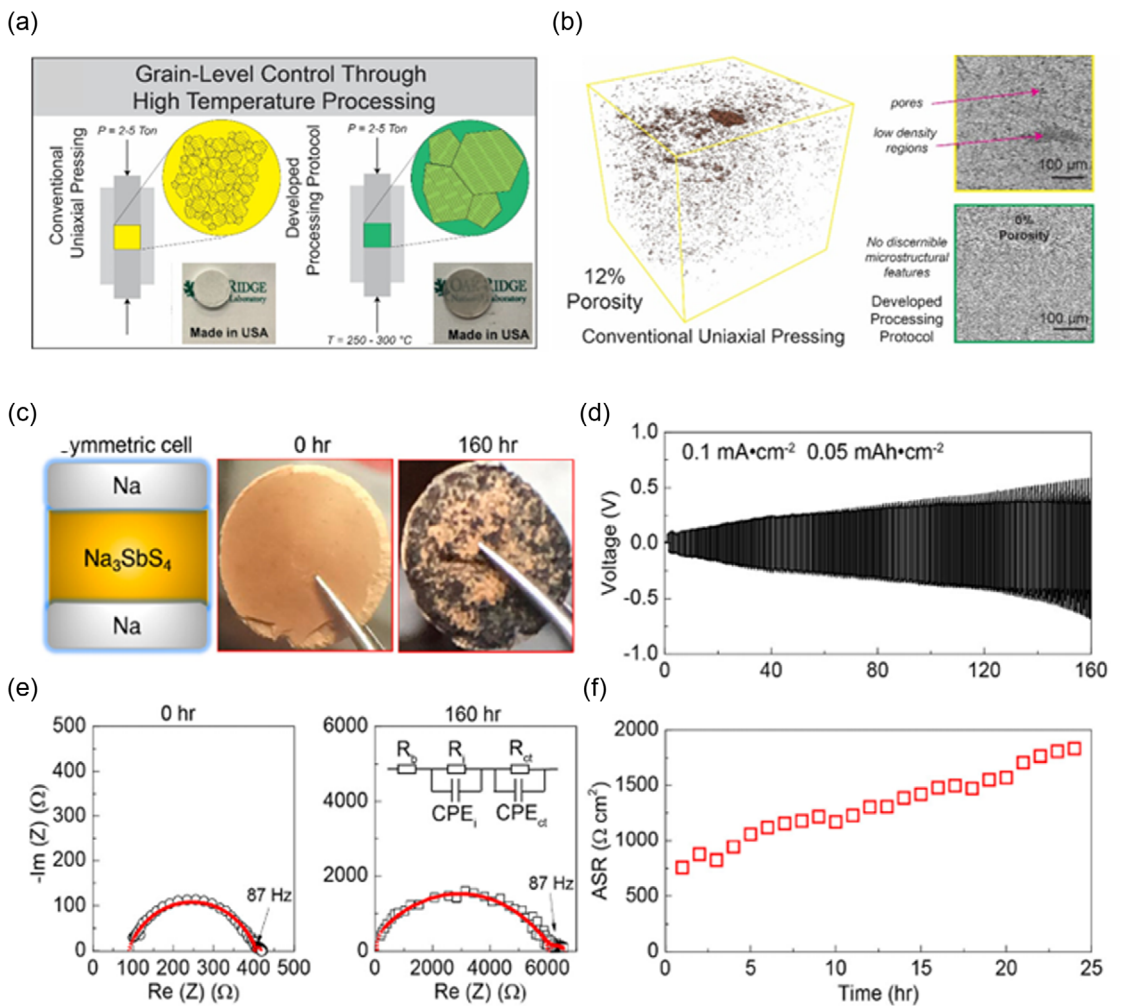


Figure 6. a) Schematic for SSE grain-scale microstructure regulation. b) Cross sectional analysis of SSE via X-ray tomography. Reproduced with permission.^[80] Copyright 2023, American Chemical Society. Characterizing Na/Na₃SbS₄ interfacial instability: c) Na/Na₃SbS₄/Na symmetric cell design and electrolyte pellet before/after 160 h operation. d) Galvanostatic cycling profile: 0.1 mA cm⁻² current density, alternating 0.5 h Na deposition/stripping cycles at 60 °C after initial 1 h rest. e) Electrochemical impedance spectroscopy (60 °C) Nyquist plots at $t = 0$ and $t = 160$ h, demonstrating rising impedance during cycling. f) ASR during the first 25 h. Reproduced with permission.^[82] Copyright 2019, American Chemical Society.

must be divided by two. A high ASR raises the overpotential, which can reduce the cell's total energy efficiency. This increased resistance can also lead to uneven nucleation during the Na ion plating process, causing localized spikes in current density and potentially leading to dendrite formation.^[84] Dominic Spencer Jolly et al. analyzed the effect of pressure on voids of Na/Na β'' alumina interface using X-ray tomography and scanning electron microscopy (SEM). The SE is shown by orange in the X-ray tomography image in Figure 7a-i, whereas the Na anode void is represented by blue. This indicates that there are tiny gaps even at the pristine interface, which suggests that the Na metal itself has some porosity. In Figure 7a, it can be seen that there are small holes present at the pristine interface, which shows that the Na metal itself has some pores. During stripping, the number and size of voids increase, while they decrease on succeeding plating at a pressure of 2 MPa and a current density of 1.5 mA cm⁻², as shown in Figure 7b-i. Figure 7j represents the pristine Na/SSE interface, and interfacial morphology after the initial plating is shown in Figure 7k, which is like the pristine Na/SSE interface (see Figure 7j) with no visible voiding. Nevertheless, tiny

holes are seen at the interface following the initial stripping (see Figure 7l). It is evident by comparing the interfaces following the initial and final stripping (see Figure 7m,n) that the void size grows noticeably with each cycle.^[85]

During stripping cycles, the interface between Na metal and Na β'' -alumina causes void formation within the Na anode. These voids slowly accumulate with the repeated cycling. This deficiency ultimately leads to dendrite growth during successive plating, causing short circuits and cell failure. Critically, this adverse process occurs above a critical stripping current density. Data shows this critical current depends linearly on applied stack pressure, strongly indicating that Na creep is the primary mechanism supplying Na to the interface. Consequently, significant stack pressures of several MPa are essential to prevent cell failure at practical current densities (several mA cm⁻²) at room temperature. For example, pressures exceeding 9 MPa are required to cycle reliably at 2.5 mA cm⁻². In summary, this work demonstrates that the Na/Na- β'' -alumina interface inherently suffers from stripping-induced void formation in the Na anode, which builds up over cycles and initiates dendrite-related failure.^[86]

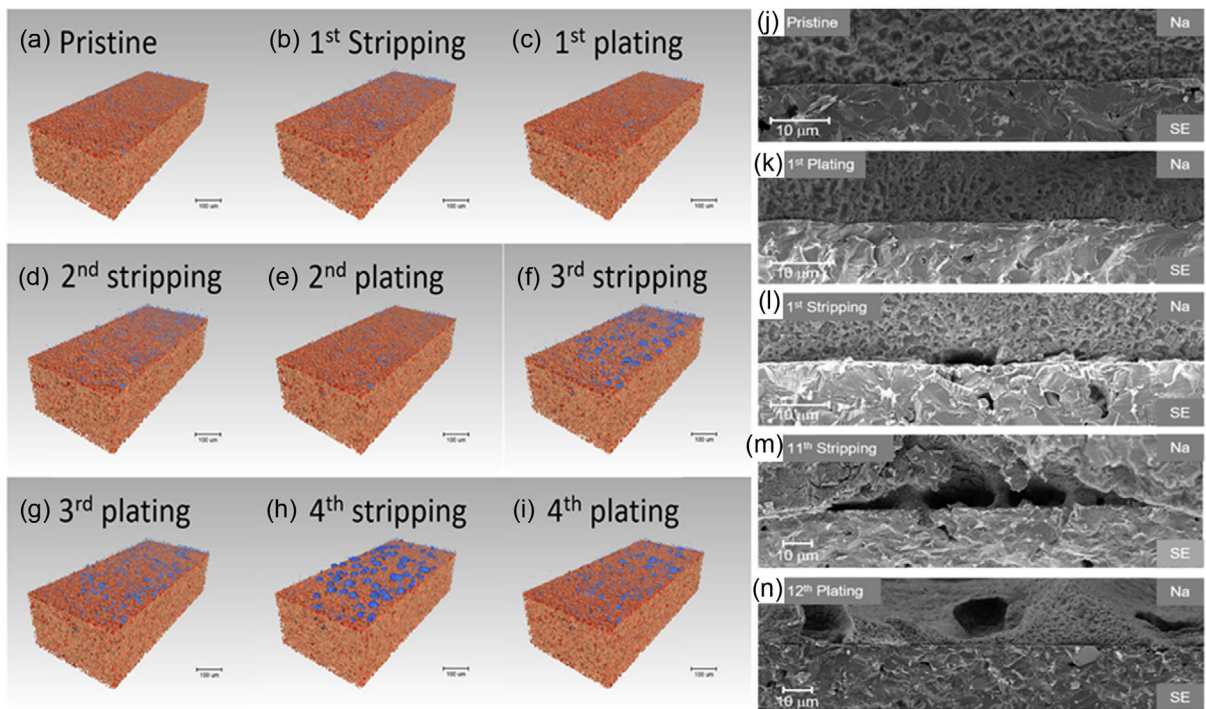


Figure 7. X-ray tomographic images of the Na/Na- β'' -alumina interface: a) pristine state; followed by cycles at b) 1st stripping, c) 1st plating, d) 2nd stripping, e) 2nd plating, f) 3rd stripping, g) 3rd plating, h) 4th stripping, and i) 4th plating. Cross-sectional SEM micrographs of the Na/Na- β'' -Al₂O₃ interface: j) pristine state; after k) 1st plating, l) 1st stripping, m) 11th stripping, and n) 12th plating. Reproduced with permission.^[86] Copyright 2020, American Chemical Society.

4.3. Interfacial Challenges on the Cathode Side

Interface formation on cathodes and SSEs mainly involves the interface between the active cathode material and the surface wetting agent, and the interface between the surface wetting agent and the SSE layer. Since many cathodes are more rigid than Na metal anodes, they make poor point-to-point contact with SSEs, which leads to sluggish transport kinetics.^[87] Additionally, due to the volume change during charging/discharging, especially during the conversion process, there is a mechanical failure of the cathode interface.^[88] One of the main reasons is the sluggish ion kinetics of SSE Na batteries, which is primarily due to higher interfacial resistance at the cathode interface. Improving the interfacial contact between the cathode and SSE has received more attention than cathode/SSE chemical compatibility.

5. Critical Challenges with Solid-State Electrolytes

5.1. Low Ionic Conductivity

SSEs ideally must possess high ionic conductivity for efficient sodium-ion transport between electrodes at room temperature. Yet, their conductivity is often compromised by interfacial problems stemming from mechanical brittleness, grain boundaries, and suboptimal electrode–electrolyte engineering. Specifically, the rigid, point-contact nature of the cathode/electrolyte interface creates a major

barrier to sodium-ion movement and mass transfer processes.^[89] The inorganic Na⁺ conductive D6FD[−]-Al₂O₃ and Na₃Zr₂Si₂PO₁₂ have been frequently used as SSEs for Na-S batteries.^[86] Chi X et al.^[90] reported Oxygen doping (Na PS_{4-x}O_x, 0 < x ≤ 0.60) in Na₃PS₄-based glassy SEs which has been reported for application in RT Na-S batteries. The modified composition Na₃PS_{3.85}O_{0.15} shows enhanced ionic transport, with a conductivity of 2.7 × 10^{−4} S cm^{−1} measured at 60 °C and a low activation energy barrier of 41.5 kJ mol^{−1}. The observed increase in ionic conductivity relative to pure Na₃PS₄ is attributed to two unique consequences of incorporating oxygen into the structure. Yuxun Ren et al.^[91] reported an in situ crosslinking reaction to embed Na-ion-conducting Na thioantimonate in a protective polymer host, which shows that, in comparison to pure inorganic SEs, hybrid solid electrolytes exhibit better chemical stability and mechanical durability. But it shows lower ionic conductivity (4.7 × 10^{−5} S cm^{−1}) at room temperature. Additionally, Gaozhan et al.^[92] reported a nanosized air-stable SE (i.e., Na₁₀SnSb₂S₁₂) for SSSBs. The nano-size particles could minimize the interfacial contact resistance (3022 Ω cm²) between the electrode and electrolyte. Despite a moderate ionic conductivity of 4.5 × 10^{−3} S cm^{−1} at room temperature, the cell was able to function reversibly and stably at room temperature. Recently Steven Kmiec et al.^[93] reported a new class of Na-based oxyhalide NaNbCl_{6-2x}O_x SSE with a facile mechanical synthesis process. This SSE shows good ionic conductivity (1.03 × 10^{−4} Scm^{−1}) as compared to other halide-based (3 × 10^{−6} Scm^{−1}) SSEs like NaNbCl₆. Authors have examined how oxygen influences structure-property relationships, and the properties of Nb₂O₅ and NbCl₃O have been estimated. This comparison specifically probed the impact of oxygen bonding type (ionic versus

covalent) on $\text{NaNbCl}_{6-2x}\text{O}_x$ formation. SSEs synthesized using Nb_2O_5 exhibited higher NaCl impurity than those containing NbCl_3O . This alteration is attributed to the NbCl_3O -derived material attaining superior oxygen distribution uniformity. However, there are several key challenges, including the larger ionic radius of Na^+ (slower diffusion compared to Li^+), higher grain boundary resistance, limited carrier concentration, and rigid crystal structures, hinder ion mobility. Poor interfacial contact between solid electrodes and electrolytes increases resistance, while material instability (e.g., sulfides degrading in air or oxides being too brittle) further complicates practical use. There are several strategies researchers have adopted, including doping, nanostructuring, composite designs, interface engineering, and the choice of a small amount of LE across the interfaces to overcome these issues apart.^[94] Still, scalability and cost remain significant hurdles for commercialization.

5.2. Structural and Fundamental Factors cause Ionic Conduction

When the battery is used repeatedly, the electrochemical process captures mobile cations from the electrodes through the electrolyte and keeps them in the active materials.^[95] High ionic conductivity is required because any resistance causes a loss of charged energy when discharged. In a microscopic sense, a diffusion

process drives ionic conduction. Deconvoluting the complicated atomic migration pathways offers better knowledge of the underlying mechanisms, leading to effective material design for future improvement, even if simple ionic diffusion is merely a prerequisite for rapid, long-range ion transport.

This section focuses on the physical qualities, particularly relevant to SEs. Arrhenius plots of SSSBs are shown in Figure 8a. This indicates that the activation energy of SSE lies in the range of 0.1–0.5 eV, which is higher than LE (<0.2 eV), and at lower temperatures, SSE shows lower ionic conductivity, but as temperature increases, the ionic conductivity increases gradually due to decreases in the grain boundaries resistance. The typical tactics for engineering the crystal lattice and their influence on ion transport will be reviewed in the context of a mature understanding of ion migration. The probability of successful leaps in which an ion can travel from one stable site to the neighboring site in a statistical thermodynamic approach of rate theory is given by

$$P = e^{-\frac{\Delta G_m}{k_B T}} \quad (9)$$

where k_B is the Boltzmann constant, T is the absolute temperature, and ΔG_m is the height of the energy barrier of the so-called “bottleneck” leap, which is the rate-determining process (i.e., Gibbs free energy difference between a saddle point and a stable position).^[96]

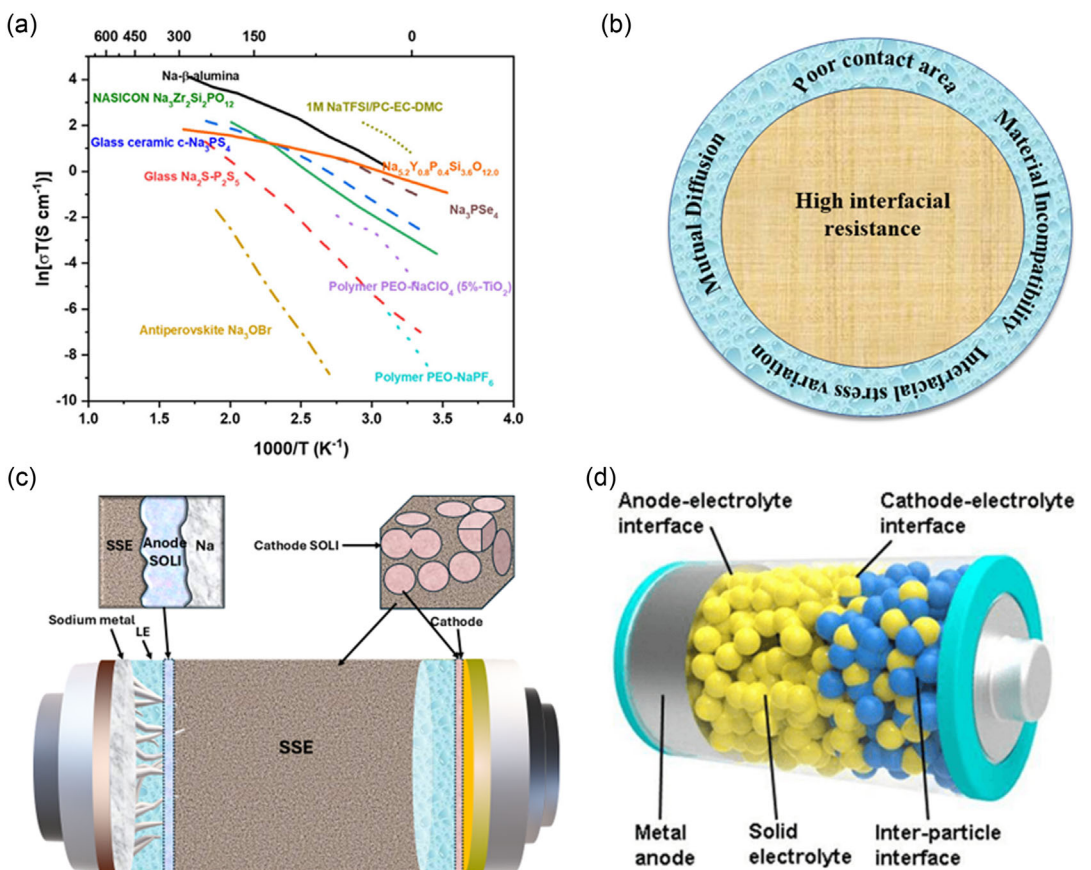


Figure 8. a) Arrhenius plots of various Na-based SSEs and comparison with conventional electrolytes. Reproduced with permission.^[142] Copyright 2023, Wiley-VCH. b) Schematic diagram providing an overview of higher interfacial resistance for the SSE. c) Schematic representation of a SOLI interfacial instability in SSBs. d) Schematic representation of different types of interfaces present in SSBs. Reproduced with permission.^[143] Copyright 2018, Elsevier.

5.3. Interfacial Resistance

SEs often have higher interfacial resistance than LEs, particularly at electrode–electrolyte interfaces. Interfacial resistance arises due to many factors, a few mentioned here: 1) mutual diffusion, 2) poor contact area, and 3) material incompatibility that leads to increased interfacial stress. The schematic Figure 8b illustrates the variation in interfacial stress. In SSE batteries, the high interfacial resistance is primarily due to the electronic and insulating nature of the cathode and its high rigidity, which does not allow point-to-point contact. In liquid-based batteries, the LEs can flow and spread easily, which helps them conduct ions well, and makes the catholyte more wettable, which could enhance its ability to conduct ions.^[97]

In order to create a composite SSE that concurrently tackles interfacial issues at both electrodes in solid-state Na-metal batteries, Fupeng Li et al.^[98] proposed a quick UV-curing technique. A competitive solvation structure is produced by adding fluorinated ethylene carbonate (FEC) to the precursor, which causes FEC to be preferentially reduced at the Na anode. As a result, a dense, NaF-rich SE interphase (SEI) is formed *in situ*, stabilizing the interphase and effectively inhibiting dendritic development. The CSE-F is directly cured on the surface at the cathode side, creating a flexible and conformal interface that can adapt to volume variations and guarantees consistent ion transport. Long-term cycle stability is improved, and interfacial resistance is greatly reduced with this dual-interface approach. As evidenced by their Na||CSE-F@NVP cell's over 2100 cycles with 91.78% capacity retention, sensible interphase and interface design are essential to the development of solid-state Na battery technology.

Furthermore Xiong Xiao et al.^[99] have successfully reduced interfacial resistance of the NZSP SSE from 28,666 to 83 $\Omega \text{ cm}^2$ using a laser etching technique. This method effectively removes interfacial impurities without using any wetting agents or stacking pressure. As a result, at 1C current density, SSE delivers a higher initial discharge capacity of 116 mAh g⁻¹ and it exhibits 68.6% capacity retention after 1000 cycles. Additionally, Yongjie Zhao et al.^[52] successfully reduced the interfacial resistance from 90 to 36 $\Omega \text{ cm}^2$ by stabilizing the Na/Na₃Zr₂Si₂PO₁₂ interface using grain-boundary engineering strategy. An optimized amount of 10 wt% Na₂B₄O was utilized as the sintering additive to enhance the densification sintering at lower temperatures. Xiong Xiao et al.^[100] recently achieved 2.284 mS cm⁻¹ ionic conductivity at 30 °C and 7.80 $\Omega \text{ cm}^2$ interfacial resistance using Ni²⁺-doped Na_{3-x}Zr_{1.8}Ni_{0.2}Si₂PO₁₂. They show that low-valence dopants (Ni²⁺, Mn³⁺) widen Na⁺ migration bottlenecks within grains and reduce barriers across grain boundaries, whereas high-valence dopants (Nb⁵⁺, Mo⁶⁺) primarily enhance Na⁺ migration along grain boundaries. The aliovalent cation substitution method leads to stable charge/discharge cycles at high rates for both symmetric Na||Na cells for 3400 h and full cells over 2400 cycles, demonstrating its practical application. Additionally, Yayu Guo et al.^[101] reported Na_{3-x}Sb_{1-4x}(SnWCaTi)_xS₄ sulfide-based SSE which shows an excellent interface stability against Na metal. The combined application of vacancy control and configurational entropy engineering yielded materials with remarkable stability against Na metal electrodes. Furthermore, these materials retained excellent stability even after direct 30 min exposure to moisture.

5.4. Compatibility and Stability

During battery operation, the integration between chemical and mechanical stability is required. A well-functioning interface in an SE and electrode necessitates rapid ion transport, optimal contact area, and chemical stability throughout the battery cycling. However, thorough investigations have revealed that electrolyte/electrode pairs previously thought to be stable can degrade due to chemical or electrochemical reactions. Numerous surface modifiers and methods have been used in recent years to form better contact between electrode and electrolyte, such as solid polymer interlayer protection, ion doping, and cold pressing methods. Additionally, interfacial stability, wettability, and contact can be improved in SSSBs by incorporating an interlayer with low electroconductivity and high ionic conductivity at the interface between the electrode and electrolyte, while interfacial impedance is reduced.^[76] This interlayer helps the formation of homogenous ion pathways, effectively suppressing dendrite formation. Concurrently, its limited electronic conductivity enhances interfacial stability and hinders detrimental side reactions at the interface. To address these interfacial issues, significant research efforts are developing novel polymer and metal oxide materials.^[102]

Figure 8c shows a schematic illustration of SOLI interfacial instability in SSBs. This configuration is typical in hybrid solid-liquid electrolyte systems, where the SSE enhances stability (preventing dendrites in Na-metal batteries) while the LE ensures efficient interfacial charge transfer. The SOLI zones are critical for minimizing interfacial resistance and maintaining electrochemical kinetics. Such designs are explored in SSBs and QSSBs to combine the safety of SSEs with the wettability of LEs, Figure 8d shows the cathode-electrolyte interface, the anode-electrolyte interface, and the interparticle interface in an inorganic SSE.

6. Challenges Associated with the SOLI

6.1. Instability and Decomposition

The SOLI is inherently reactive, and its composition can evolve due to ongoing electrochemical reactions between the Na anode and the electrolyte. This evolution may lead to the breakdown of the SOLI, causing an increase in interfacial resistance and degradation of battery performance. In particular, the LE component is prone to continuous decomposition, which can deplete the electrolyte and alter the SOLI's structure. Bin et al. reported three types of interfaces present in SSBs.^[103]

Type I—A thermodynamically stable interface where no electrochemical or chemical reactions take place.

Type II—An ion passivating interface that conducts both ions and electrons, termed as mixed ionic electronic conducting interphase (MCI).

Type III—A steady solid (or cathode) electrolyte interphase (SEI or CEI) with high ionic conductivity but insignificant electronic conductivity.

For long-term stable battery operation, there is a need for type I or type III interfaces. In the second case, when there is

inadequate contact, high interfacial resistance is typically found, which has a detrimental influence on the cell's cycling performance. In addition, the substantial decomposition of the SOLI leads to "chemo-mechanical" effects that damage its mechanical stability. This instability results in uneven deposition of anodic metals, which increases stress on the SEI layer.^[104] In sulfide-based SSE, the main components of mixed ion-electron conduction products of the SOLI layer are Na_3Sb , Na_2S , and Sb, which promote the continuous decomposition of Na_3SbS_4 , and the symmetric battery polarization gradually increases.^[105]

6.2. Nonuniform Deposition and Mechanical Integrity

The formation of a uniform SOLI across the entire Na anode surface is critical for effective dendrite suppression and ion transport. However, nonuniform deposition of electrolyte decomposition products can lead to localized areas of high resistance or weak points where dendrites can penetrate. Achieving a homogeneous and defect-free SOLI remains a significant challenge. The mechanical properties of the SOLI, particularly its ability to resist dendrite penetration and accommodate volume changes during cycling, are critical for battery longevity. If the SOLI is too rigid, it may crack under the strain of volume fluctuations, leading to failure. Conversely, if it is too soft, it may not provide sufficient protection against dendrite growth.

Jin et al.^[106] shows how sodium SSE contact degrades during stripping/plating cycles due to significant dimensional changes. During stripping, voids develop at the SOLI interface, reducing contact area and forcing preferential ion flux toward better-connected regions. This uneven flux distribution causes irregular stripping/plating that ultimately triggers dendrites. The void-refilling capability ($J_{\text{replenishing}}$) combines metal diffusion flux ($J_{\text{diffusion}}$) with stress-driven creep void elimination. When stripping flux (J) exceeds $J_{\text{replenishing}}$, voids automatically expand and damage Na/SOLI/SSE contact. At lower current densities (J_{strip}), the interface maintains integrity as slow metal depletion allows $J_{\text{replenishing}}$ to instantly refill voids. However, higher J_{strip} rates overwhelm replenishment capacity, making voids prominent as shown in Figure 9a.^[86] During plating, ions redeposit starting at SSE-metal-void junctions before spreading across void surfaces. Unfilled voids reduce contact area, and repeated cycling accumulates interfacial voids and "dead metal" that progressively degrade Na/SOLI/SSE contact, see Figure 9b.

6.3. Chemical Stability with Electrolytes

The chemical compatibility between the SOLI and both the liquid and SE components is crucial for long-term stability. Incompatible materials may lead to the dissolution of the SOLI into the electrolyte or undesirable reactions that degrade the battery's performance. Na-based SSE shows better deformability and have very

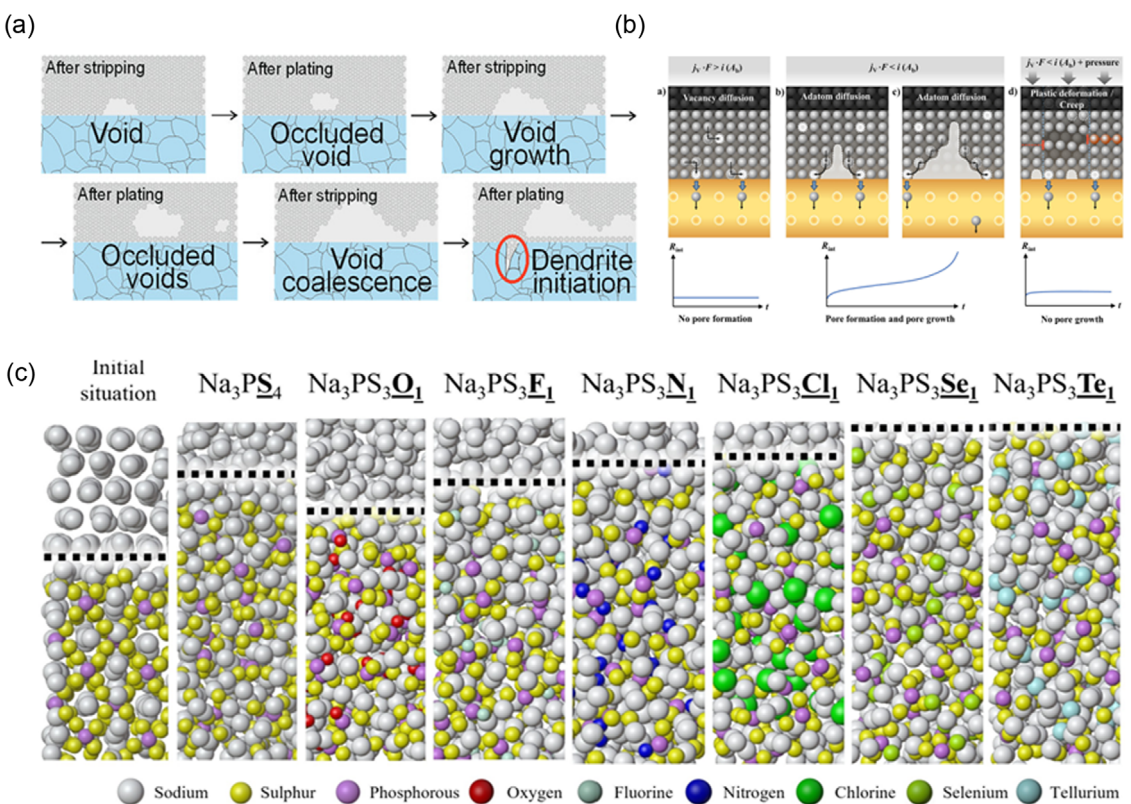


Figure 9. a) Void formation mechanism at the metal/SSE interface. Reproduced with permission.^[86] Copyright 2019, American Chemical Society. b) Metal replenish mechanism and the corresponding interface resistance profile. Reproduced with permission.^[106] Copyright 2020, Elsevier. c) Initial and end-of-simulation snapshots at 400 K for all PS_3X_1 types. Reproduced with permission.^[110] Copyright 2018, American Chemical Society.

high Na-ion conductivity at room temperature, but due to chemical stability, they face several challenges.^[107,108] However, there are very less studies available related to chemical studies for Na-SSE batteries. It is tough to explore this area from an experimental point of view, especially in *operand mode*. Additionally, limitations in computer power cause significant difficulty when simulating a high number of atoms at the interface. For instance, sulfide-based SEs tend to be highly air- and water-sensitive, reacting with moisture to produce poisonous H₂S gas through hydrolysis. In contrast, oxide-based SEs generally reveal better stability in air and moisture, allowing safer handling and more reliable performance under ambient conditions.^[109]

A particular Na₃PS₄ SSE electrolyte is surrounded by regularly spaced PS₄ groups in which Na ions are loosely bound and can migrate freely. It was revealed that when Na atoms were exposed to the Na metal electrode, they would approach and break the P—S bonds inside the PS₄ groups one at a time, resulting in the production of PS₃, PS₂, PS₁, and eventually phosphide and sulfide species. Different design ideas have been proposed in many studies to further improve the chemical stability against the Na metal electrode. Lieven et al.^[110] proposed a simulation study for Na metal and the Na₃PS₃X₁ (where X is S, O, F, Cl, N, Se) electrolyte using neural network molecular dynamics which was performed at 400 K as shown in Figure 9c in which the dashed line indicates the estimated interfacial degradation boundary. At the boundary of SOLI, Na metal electrodes were very reactive and mobile, so they were able to move through the Na₃PS₃X₁ solution and raise the breakdown limit. Oxygen provided the greatest stability toward the Na metal electrode, surpassing that of sulfur out of all materials, as shown in Figure 9c. The degree of degradation for other heteroatoms increased from sulfur to fluorine, nitrogen, chlorine, selenium, and finally tellurium, depending on the chemical properties of the respective elements. Lieven Bekaert et al.^[110] found that the slow diffusivity of Na is not a fundamental reason for the suppression of decomposition. They found that in the case of oxygen, the P—O bond was found to be very stable, but for sulfur, there was a sequential breakdown of P—S bonds. The P—Cl, P—Se, and P—Te bonds were the first to break for chlorine, selenium, and tellurium, respectively. This is probably because the heteroatoms have a larger atomic radius, which makes the bonds longer and makes it easier for Na metal atoms to react with them. The larger atomic radius also makes the electrolyte not work well with the heteroatoms.

7. Strategies to Overcome the Challenges Associated with the SOLI

7.1. Electrolyte Engineering

Careful design of the electrolyte composition, including the choice of LE additives and SE materials, can help to control the formation and stability of the SOLI. Additives such as fluorinated solvents or ionic liquids can enhance the mechanical strength and ionic conductivity of the SOLI while minimizing side reactions. Currently, the most widely used LEs are mainly classified into organic electrolytes,

ionic LEs, and aqueous electrolytes, depending on the solvents used.^[111,112] Linear carbonates (dimethyl carbonate, DMC; ethyl methyl carbonate, EMC; diethyl carbonate, DEC), ethers (diglyme and triglyme), and cyclic carbonates (ethylene carbonate, EC; propylene carbonate, PC) are commonly used organic solvents in the formation of SOLI in SSE because all these exhibit good electrochemical stabilities and ion transport abilities.^[31] Various types of organic solvents are commonly used to create binary or multi-component solvent mixtures that effectively suppress dendrite formation, enhance thermal stability, and expand the electrochemical window of the electrolyte.^[113] Sulfide-based SSE efficiently reacts with LEs and forms unwanted products like polysulfides or some complex compounds compared to oxide-based SSE. In contrast, the fluoride-based LEs are the most robust in terms of oxidation stabilities with SSE, and they have been found to enable the effective suppression of Na dendrite growth by forming a NaF-based SOLI when in contact with the Na anode.^[114,115] Additionally, the hybrid interphase of NaF/Na₃Sb significantly reduces the surface reactivity and interfacial impedance. Recently, Zhendong Yang et al.^[54] introduced SnF₂ film onto the surface of Na_{3.2}Zr_{1.9}Ca_{0.1}Si₂PO₁₂ (NZSP) to improve interfacial contact, where SnF₂ is a composite conductive layer containing Na_xSn alloys and NaF at the interface. As a result, the interfacial resistance between Na/NZSP drastically decreases (813 to 5 Ω cm²) and critical current density increases (1.8 to 0.2 mA cm⁻²). At 30 °C, the symmetric cell can cycle stably at 0.2 mA cm⁻² for 1300 h.

Jiayi Yang et al.^[116] successfully deposited SnO_x/Sn thin film using magnetron sputtering, and as a result, the interfacial resistance between Na/NZSP is dramatically reduced from 581 to 3 Ω cm². At room temperature, Na||Na symmetric cell stably cycles over 1500 hr with an overpotential of 40 mV at 0.1 mA cm⁻². Since they have used magnetron sputtering to deposit SnO_x/Sn thin film, we cannot use this approach for large-area applications. Additionally, the use of multiphase interphases, comprising both inorganic and organic components, can help to balance the mechanical strength and flexibility of the SOLI by incorporating both stiff, dendrite-resistant materials like NaF and ductile materials that can accommodate volume changes, which helps to achieve a more robust and stable SOLI.

7.2. Techniques to Characterize SOLI

Understanding the composition and structure of the SOLI is key to optimizing its performance. Advanced characterization techniques, such as X-ray photoelectron spectroscopy (XPS), scanning electron microscopy (SEM), scanning transmission X-ray microscopy (STXM), and X-ray absorption spectroscopy (XAS), can provide insights into the formation mechanisms and evolution of the SOLI over time, enabling targeted improvements in its design. Shuo Yan et al.^[117] employed a combination of scanning transmission X-ray microscopy (STXM), ptychography, and X-ray absorption spectroscopy (XAS) to probe the origins of capacity fade at the nanoscale. This multitechnique synchrotron approach qualitatively analyzed a hybrid garnet-based SSE paired with an the Ni_{0.6}Mn_{0.6}Co_{0.2}O₂ (NMC 622) cathode at the nanoscale. In this

research, direct evidence of substantial cavities in NMC 622's secondary particles has been obtained as shown in **Figure 10**. The researchers hypothesized "that the holes in the material could be used as a way for LE to pass through the cathode, which would lead to less material being present and more cations dissolving in a special kind of battery called SS-LMB that has a cathode made of Li-Ni_{0.6}Mn_{0.6}Co_{0.2}O₂ (NMC 622)." More importantly, the defective cathode is unable to maintain its structural and chemical stability, resulting in a capacity loss during the initial stages of battery cycling. Images in Figure 10a,b show a void that seems to traverse a spherical secondary particle (an aggregate of primary particles) and accompanying cracks, potentially formed during cathode laminate fabrication. Examination of primary particles after one cycle shows no evident cracks (Figure 10c). In contrast, secondary particles from NMC_28 exhibit no large pores (Figure 10d). Nevertheless, white arrows in Figure 10e point to fine intergranular fissures starting at the surface and extending inward along grain boundaries. More microcracks are visible in

the core region (Figure 10e) separating differently aligned primary particles. Additionally, intragranular cracks are developing within some primary particles, as marked by yellow arrows in Figure 10f. The formation of these microcracks is likely a synergistic outcome of continuous oxygen release, internal microstrain, and anisotropic volume shifts during lithium removal and insertion.

Additionally, SEM can be used to analyze the SOLI in SSBs, taking the electrode surface images before and after the cycle to see the voids and cracks available on the electrolyte surface. Junxiong Wu et al. reported Na trifluoromethanesulfonimide (NaTFSI) in a mixture of trimethyl phosphate (TMP) and fluoroethylene carbonate (FEC) for a dendrite-free Na-S battery.^[118] Figure 10g shows that the addition of FEC not only promotes the formation of stable NaF-rich SOLIs at the Na anode side but also helps to stabilize the cathode/electrolyte interface for RT Na-SSE batteries.^[118] Furthermore, using XPS, we can analyze the chemical composition of the SOLI, including the presence of

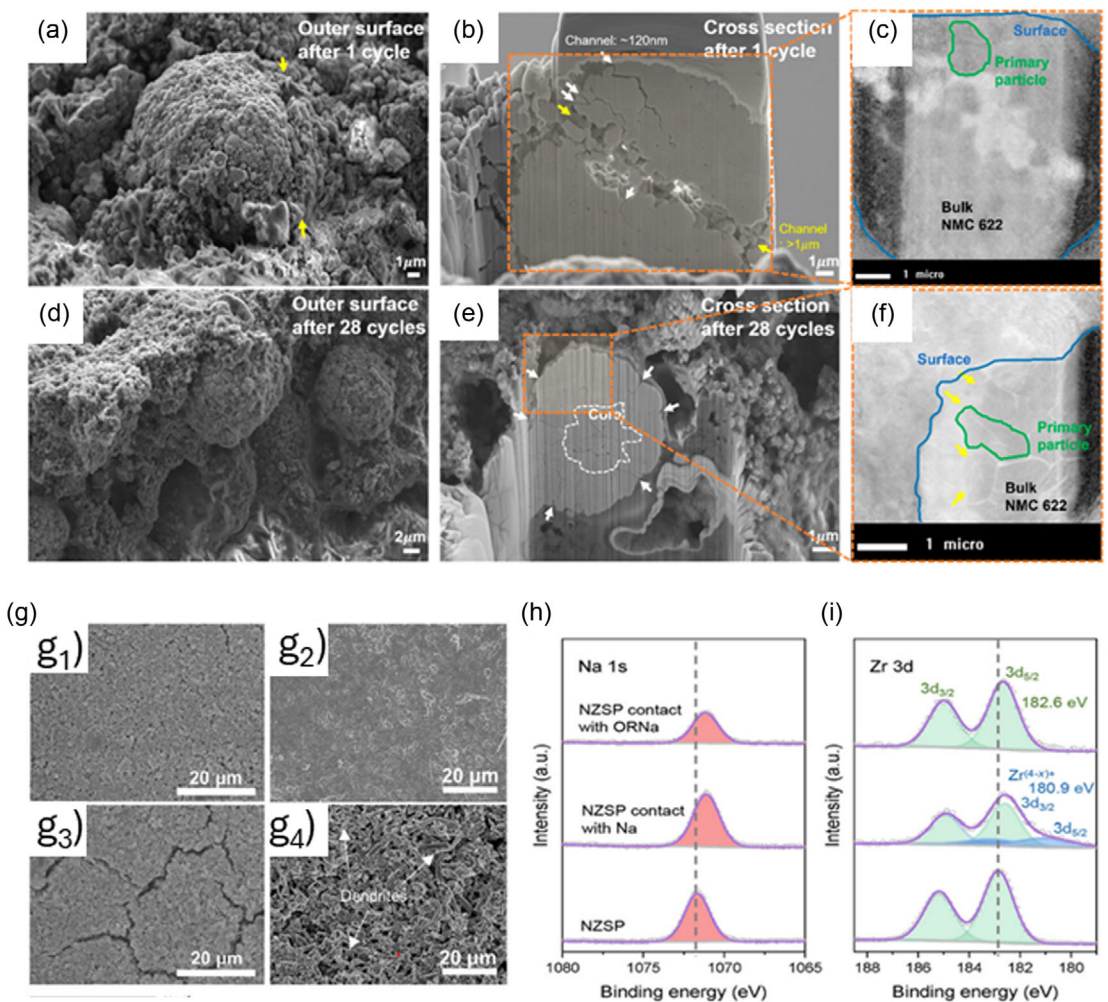


Figure 10. NMC 622 characterization: a) FESEM after 1 cycle; b) cross-section after 1 cycle; c) HR-STXM detail of (b); d) top view after 28 cycles; e) cross-section after 28 cycles; f) HR-STXM detail of (e). Reproduced with permission.^[117] Copyright 2023, American Chemical Society. FESEM micrographs of the sulfurized polyacrylonitrile cathode after 100 cycles in electrolytes (g₁) with and (g₂) without FEC. SEM images of Na surface after 50 cycles in electrolytes (g₃) with and (g₄) without FEC. Reprinted with permission.^[118] h) Na 1s, i) Zr 3d XPS spectra of NZSP before and after contact with Na and ORNa. Reproduced with permission.^[119] Copyright 2024, Elsevier.

Na, oxygen, carbon, and other elements. Recently, Keshuang et al.^[119] demonstrated oxygen-regulated spontaneous SEI for Na–Na₃Zr₂Si₂PO₁₂ (NZSP) SSE, in which XPS characterization shows its chemical states of composing elements for SEI in Na–NZSP. Figure 10h,i shows the binding energies of Na and Zr on both Na–NZSP and oxygen-rich Na–NZSP surfaces before and after contact show and it shows a shift to lower energy, indicating that the SOLI layer is composed of a partially reduced NZSP surface.

7.3. In Situ Operando Analysis: A General Overview

As the electrode–electrolyte interface of an SSE functions as a critical area, unraveling advanced characterization and analytical tools for better understanding are to be employed.^[29] Interfacial engineering through the SOLI approach enables accelerated ion movement, thereby reducing interfacial resistance, ensuring uniformity in Na plating and striping; hence, a dendrite-free, long-term, cyclable battery is constructed.^[120] However, since ion movements are restricted through resistive pathways in ASSBs, researchers have developed approaches to address this issue.^[121] Electrolyte engineering through additive incorporation and functional additives, solvation tweaking, plasticizing the matrix, and advanced hybrid electrolytes such as QSPEs has been explored.^[22,122] Multiple processes are initiated at the interface with the progression of galvanostatic charge–discharge cycles in an SSB. It involves the dynamic evolution of interfacial contact and space charge layer formation, the evolution of SEI, the morphology of Na deposition, and the formation of dendritic structures.^[123,124] As ex situ analysis unveils the processes and mechanisms after cycling the SSE-based cells, the dynamic changes during cycling remain hidden. Hence, the necessity of in situ/operando techniques for the dynamic analysis at the interfaces is being explored by researchers.^[125]

7.3.1. In Situ Microscopy Techniques

Information on the dynamic growth of dendrites can be visualized through in situ microscopic analysis. In this regard, in situ optical microscopy is a simple yet effective technique for analyzing the effect of Na deposition.^[126] Hence, optical cell design principles have been developed in the case of LE-based SMBs.^[127] It is well established that the plating/stripping profile exhibited by a cell can provide insight into the possibility of dendrite formation, the stability of SEI, and overall battery performance.^[128] For instance, Yadav et al.^[127] investigated the effect of solvation structure and its correlation with SEI formation and dendritic growth by employing an in-house fabricated optical cell. Correlation of Na dendrites and salt anion molecules was analyzed through the overpotential values of Na plating/stripping profile, SEI compositional analysis with XPS, and investigating dendrite formation through an optical cell. The study employed NaCF₃SO₃ salt, NaPF₆ salt, and NaClO₄ salt. The real-time dendrite formation was visibly high in the case of NaClO₄ salt, followed by NaPF₆ salt, and was least observed for NaCF₃SO₃ salt (Figure 11). This was evidenced

by the plating/stripping profile, where the cell with NaCF₃SO₃ salt exhibited the least overpotential. Furthermore, as the solvation of Na salt molecules also regulates SEI,^[28] the investigators also correlated this aspect. It was found that diglyme (G2) with NaCF₃SO₃ salt displayed the most stable and compact solvation structure, which contributed to a robust inorganic-rich SEI.

Advanced microscopic analysis has also been investigated in SMBs.^[126] In this regard, in situ TEM analysis is considered a complex technique as it can open the avenues to unveiling the multi-scale electro-chemo-mechanical evolution.^[129] For instance, Jia et al. employed in situ TEM in a Na–oxygen battery,^[130] which is classified under the SMB category.^[131] As the morphology of cathode discharge products and their formation regulate the electrochemical performance of the metal-air batteries,^[132] in situ TEM revealed the effect of the catalyst on the oxygen reduction and the oxygen evolution reaction. In another work, Zhang et al.^[133] conducted in situ TEM analysis to analyze sodiation and desodiation processes for a Na battery with gel polymer electrolyte. A combination of in-situ analyses can unveil the dynamic processes in a battery. Daali et al.^[134] conducted a study employing in situ (SEM), in situ synchrotron X-ray absorption spectroscopy (XAS), and XPS in a Na-ion battery. The study was focused on unraveling complex electro-chemomechanical behavior while the cell is in charging–discharging conditions. Moreover, in situ transmission electron microscopy (TEM) is increasingly being used in the field of ASSBs to visualize cathode deterioration and interface failure in real time. Zheng et al. demonstrate in this thorough analysis how in situ TEM allows for the direct observation of phase transitions, ion migration, interfacial reactions, and structural evolution in cathode active materials and their interfaces with SSEs across a variety of ASSB types. The authors demonstrate how this method captures characteristics that are frequently overlooked in postmortem analysis, such as phase borders, space charge layers (SCLs), volume changes, and microcracking during battery operation. They describe how metrics, including ion transport paths, charge density, and valence state mapping, can be spatially and temporally resolved at the nanometer scale using sophisticated TEM modes like STEM-EELS, DPC, and electron holography. Crucially, this degree of resolution enables researchers to detect mismatched lattice structures, differentiate between surface and bulk behaviors, and assess how these problems result in mechanical failure and poor ionic conductivity.^[135]

Although in situ optical microscopy analysis, which involves a simpler experimental setup, has been introduced, complex analyses such as TEM and SEM have not been widely explored. Specialized chambers are to be designed to ensure isolation from the ambient atmosphere.

7.3.2. In Situ X-Ray Techniques

Looking beyond the surface—literally—becomes crucial when trying to figure out what actually controls SSB performance. The work by Lucero et al. is a crucial contribution in this regard since it examines the use of in situ synchrotron X-ray techniques

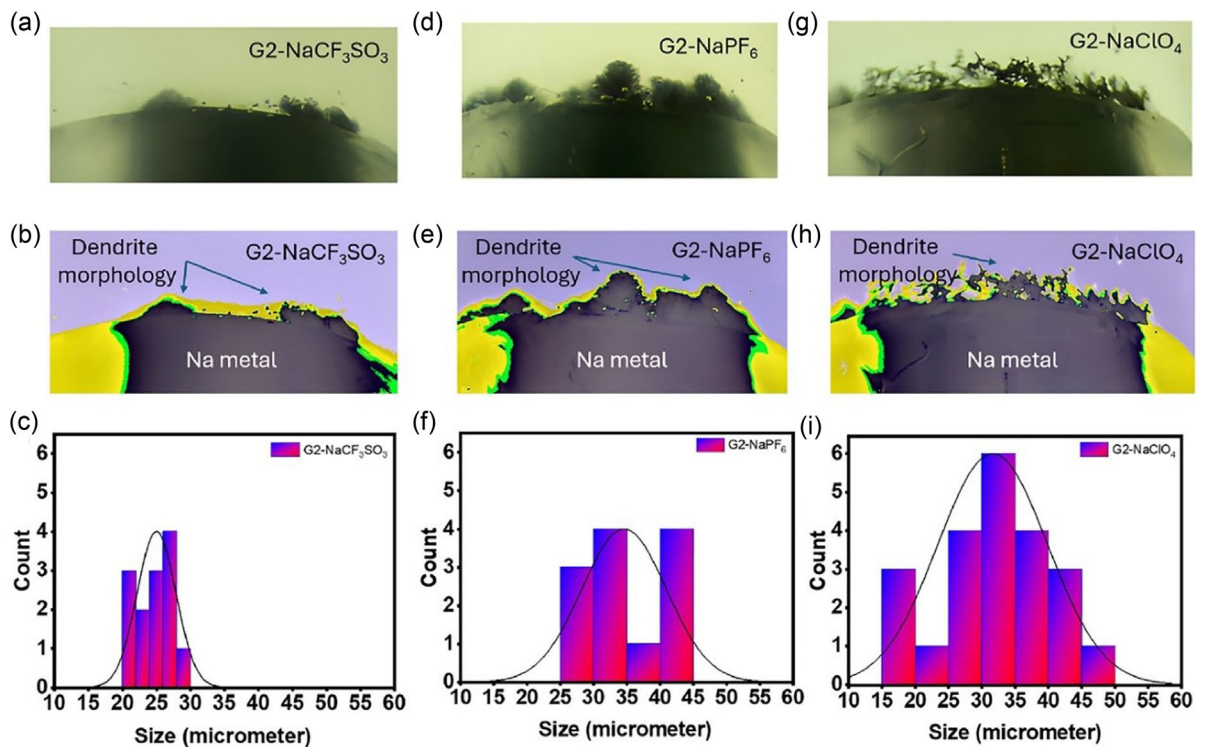


Figure 11. Results from in situ optical microscope analysis, Na dendrites formation, its processed images, and dendrite distribution a) Na cell with electrolyte as diglyme (G2) with NaCF_3SO_3 salt, b) processed image using ImageJ software, c) dendrite size distribution graph, d) Na cell with electrolyte as diglyme (G2) with NaPF_6 salt, e) processed image using ImageJ software, f) dendrite size distribution graph, g) Na cell with electrolyte as diglyme (G2) with NaClO_4 salt, h) processed image using ImageJ software, and i) dendrite size distribution graph. Reproduced with permission.^[127] Copyright 2024, Elsevier.

to investigate and comprehend the intricate solid–solid interfaces in SSBs, which are otherwise challenging to reach. Advanced synchrotron-based techniques, including X-ray diffraction (XRD), surface XRD (SXRD), XAS, and XPS, allow for real-time monitoring of interphase formation, interface reactions, lattice distortions, and changes in chemical composition during battery operation. These techniques enable researchers to collect depth-resolved information regarding changes in electronic structure, oxidation states, and lattice integrity in addition to identifying which phases or compounds are developing at interfaces. These techniques also show how buried interfaces change structurally and chemically over time, establishing a clear link between battery performance and interfacial stability. For instance, cathode–electrolyte interfaces, including layered oxide cathodes and glass–ceramic electrolytes, were examined using depth-resolved XAS. In these cases, the introduction of a thin interlayer, such as NbO_2 , helped to reduce local structural distortions. Without this interlayer, transition metals like cobalt experienced undesired oxidation state shifts close to the interface, which were associated with increased interfacial resistance and structural instability. These case studies show how in situ methods can identify the pathways of degradation and offer design guidelines for interphase stabilization.^[129] Fehse et al. also gave an appealing overview of how contemporary synchrotron-based X-ray spectroscopy methods are revolutionizing our capacity to examine the inner workings of batteries, particularly solid-state ones. Their function in characterizing buried solid–solid surfaces, like the electrode–electrolyte interfaces

and the SEI, is especially significant because these interfaces are essential to the long-term safety and performance of SSBs. The authors stress that real-time operando probing is essential since these interfaces are frequently only a few nanometers thick and dynamically change during cycling. These X-ray techniques aid in quantifying degradation pathways, electronic structure changes, and ionic mobility by providing depth- and time-resolved insight into both surface and bulk phenomena. These techniques are essential for assessing and improving battery performance metrics like stability, reversibility, and interfacial resistance.^[136]

7.3.3. In Situ Raman Spectroscopy

Lin et al. discuss the critical role of in situ Raman spectroscopy, a vibrational method that can identify molecular structure, plays within revealing mechanisms in rechargeable batteries. The authors stress that during electrochemical cycling, structural, phase, and lattice changes in electrode materials can be monitored using in situ Raman. This makes it easier to see processes like phase transitions and ion intercalation. The finding of important vibrational signals from such processes is made possible by Raman's spectrum specificity, which provides molecular-level understanding of energy storage and degradation mechanisms. In addition, they highlight core–shell nanoparticle-enhanced Raman spectroscopy (like SHINERS), which increases the accessibility of buried

processes by amplifying weak interfacial signals from ultra-thin layers like electrode–electrolyte interfaces or solid electrolyte interphases (SEI). The ability to extract crucial metrics, including intermediate species, redox-active sites, and interfacial stability—all essential for directing material and interface design for high-performance batteries—is made possible by the combination of high sensitivity and surface specificity.^[137] Moreover, it needs not just sophisticated materials but also sophisticated instruments that can record the dynamic evolution of SSBs to understand where and how they fail while in use. Zhang et al. reviewed the application of *in situ* and *operando* Raman spectroscopy (IS/O-RS) to monitor the molecular and interfacial behavior of components inside all-solid-state lithium batteries (ASSLB) thoroughly. The author illustrates how IS/O-RS enables researchers to directly monitor electrode–solid electrolyte interfaces, electrode structural transitions, and SE disintegration under realistic cycle settings because of its molecular sensitivity and nondestructive nature. For example, the study's highlighted findings demonstrate how IS-RS captures different Raman shifts (e.g., from PS_4^{3-} to $\text{P}_2\text{S}_6^{4-}$ or elemental sulfur) to identify phase transitions and breakdown products at cathode–electrolyte interfaces such as NCM811|LPSC or LCO|LPSC. This offers firsthand knowledge of the processes underlying interfacial deterioration. When in contact with Li metal, IS-RS on the anode side allows for the real-time identification of sulfide reduction products such as Li_2S or CuS , which aids in mapping the reductive instability of sulfide electrolytes. In order to get over restrictions like limited signal strength at buried contacts, the study also covers Raman augmentation techniques like SHINERS and TERS. The study concludes that IS/O-RS is an essential tool for resolving bulk transformations, interface dynamics, and interphase chemistry, all of which are crucial for maximizing the lifetime and performance of ASSLBs.^[138]

7.3.4. Other Operando Techniques for Battery Materials

Tripathi et al. highlighted the value of *in situ* and *in operando* analytical methods in revealing the dynamic structure, chemistry, and evolution of the cathodic electrolyte interface (CEI) and solid–electrolyte interface (SEI), two essential layers that control battery longevity, performance, and safety. In order to track phase changes, gas evolution, compositional shifts, and mechanical degradation at the interface, the study methodically explains how instruments like XRD, XAS, XPS, Raman, FTIR, ellipsometry, and others are modified for *in situ* use. Specifically, how vibrational spectroscopies like *in situ* FTIR and Raman show organic and inorganic SEI species in real time, whereas synchrotron-based XAS and XRD identify SEI growth, lattice alterations, and ion intercalation interactions. Critical characteristics that affect impedance, Coulombic efficiency, and irreversible capacity loss, such as SEI thickness, component distribution, and structural integrity, can be quantified with the aid of these techniques. The paper also emphasizes how these same methods may be used to study and manage interfacial interactions in artificial SEIs, which are created coatings that mirror natural SEI but have greater stability.^[139]

8. Summary and Perspective

In summary, we have comprehensively discussed the importance of the SOLI in SSBs. We highlighted the critical factors impacting the performance SSSBs. The SOLI serves as a vital component in current SSBs, significantly influencing the performance of SSSBs by enhancing ion transport and reducing interfacial resistance. The key aspects of SOLI comprise the chemical and mechanical stability of the electrolyte, the ionic conductivities of the electrolyte, and the interfacial resistance affected by the wettability of the electrolyte. Still, challenges like electrochemical stability, uniform distribution, and the compatibility of the LE with the SE restrict the practical usage of SSSBs. The mechanical incompatibility at the electrode–electrolyte interface presents a significant challenge. If not properly addressed, it can result in volume changes during charging and discharging, leading to delamination of the electrode materials, the protective coating layer, or both. The emergence of cracks and voids at the interface plays a significant role in the ongoing degradation observed during cycling. The presence of these structural defects reveals new electrode surfaces to the SE, initiating further chemical and electrochemical reactions that diminish cycling efficiency and capacity.

The SOLI serves as a protective barrier, effectively preventing direct interaction between the highly reactive Na metal and the SE. A stable SOLI can manage the volume changes that happen during the processes of Na deposition and stripping. The combination of solid and liquid elements in the electrolyte contributes to the development of a more resilient interphase. The SOLI effectively stabilizes the surface of the Na metal anode and the SE by passivating them, thereby restricting the occurrence of undesirable side reactions. The regulation of Na deposition and the enhancement of inorganic components within the SOLI contribute to increased mechanical strength, thereby assisting in the reduction of dendrite formation.

Furthermore, most SSEs (including sulfides, oxides, and halides) are unstable in proximity to the Na-metal anode and thus chemically/electrochemically react to form the SE interphase.^[140,141] The interfacial resistance issue between the SE and Na metal anode can be effectively mitigated by developing the SE directly on the anode's surface through *in situ* growth techniques employing volatile compounds (see Figure 12a). Additionally, the capacity and stability of SSBs can be significantly improved by stacking nanoparticle layers between the electrodes (see Figure 12b). The introduction of various active materials into the electrode layer can lead to a substantial enhancement in battery capacity. For example, the layer of the positive electrode is composed of an active material specific to the positive electrode and SEs, which function as a pathway for ionic conduction. Thus, to realize SSSBs, it is necessary to develop a SE exhibiting high ionic conductivity and an electrode material with a high capacity.

Additionally, for oxide-based SSEs, high-temperature annealing is necessary to wet the interface chemically. To improve the contact and prevent Na dendrites, techniques such as cold pressing malleable Na on the SE surface, Na–K alloys, thin polymeric films (PVDF-HFP, PEO-PVDF-HFP, PMA-PEG, PVDF-PVP, PEO-PAN) (see Figure 12c), improved interlayers with high ionic

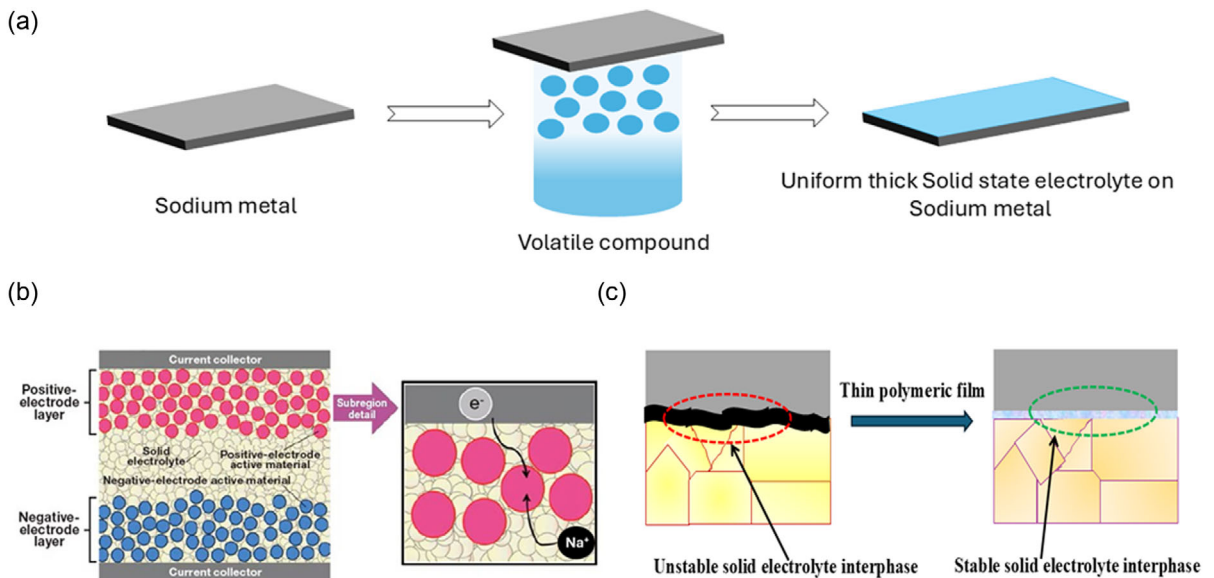


Figure 12. a) Schematic illustration of the direct growth of the SSE on the Na metal anode. b) Bulk-type all-solid-state battery. c) Introducing a thin polymeric film between interphases.

conductivity, low electronic conductivity, and high compatibility are developed. The main concern for Na-based SSBs is creating a good ionic contact between the electrodes and the SE with minimum side reactions. The interfacial properties in SSBs are constantly influenced by the cathode's volume instabilities and the dendritic growth on the Na-metal anode.

Further research should concentrate on several critical areas to advance the practical use of room-temperature SSBs. First, while it's important to improve the current structures for better stability at the interfaces, we also need to explore new structures that provide high ionic conductivity and better chemical and electrochemical stability. Future studies should draw guidance from fundamental principles and theoretical models. Additionally, several approaches are recommended to enhance the physical and electrochemical stability of SSEs: 1) Direct growth of the SE on the Na metal anode through in situ growth techniques. 2) Minimize the particle size of electrolytes to enhance surface area and improve interfacial contact, thereby aiding in the reduction of interfacial resistance and mechanical stress. 3) Increase in ionic conductivity by doping the materials or adjusting the synthesis parameters. 4) Introduction of inorganic SEs with polymers or ionic liquids to improve mechanical flexibility and interfacial contact. 5) Refinement of sintering parameters or incorporation of additives to enhance grain boundary interaction, thereby improving ionic transport and mitigating crack formation at grain interfaces.

In conclusion, enhancing the physical and electrochemical stability of SSEs is crucial for the progression of all-SSB performance. The SOLI is essential in influencing interfacial resistance, chemical stability, and the efficiency of ion transport. Approaches like interface engineering, doping, composite design, and nanostructuring play a crucial role in stabilizing this interphase and facilitate safer and high-capacity energy storage systems.

Acknowledgements

R.S. and V.K. acknowledge the financial assistance provided by Department of Science and Technology (DST), the ISRO, and the Indian Institute of Technology Delhi (IIT Delhi). Tushar, V.S.K., and V.K. would like to thank IIT-Delhi, India and UQ, Australia, for the collaborative program, UQIDAR for the support.

Conflict of Interest

The authors declare no conflict of interest.

Keywords: electrolyte engineering • interfacial resistance • sodium metal batteries • solid electrolyte interfaces • solid electrolytes

- [1] A. Nasu, T. Otono, T. Takayanagi, M. Deguchi, A. Sakuda, M. Tatsumisago, A. Hayashi, *Energy Storage Mater.* **2024**, *67*, 103307.
- [2] Sungjammenla, S. K. Vineeth, C. B. Soni, V. Kumar, Z. W. Seh, *Energy Technol.* **2022**, *10*, 2200421.
- [3] E. Fan, L. Li, Z. Wang, J. Lin, Y. Huang, Y. Yao, R. Chen, F. Wu, *Chem. Rev.* **2020**, *120*, 7020.
- [4] O. B. Chae, B. L. Lucht, *Adv. Energy Mater.* **2023**, *13*, 2203791.
- [5] X. Yu, A. Manthiram, *Energy Environ. Sci.* **2018**, *11*, 527.
- [6] J. Liu, Z. Bao, Y. Cui, E. J. Dufek, J. B. Goodenough, P. Khalifah, Q. Li, B. Y. Liaw, P. Liu, A. Manthiram, Y. S. Meng, V. R. Subramanian, M. F. Toney, V. V. Viswanathan, M. S. Whittingham, J. Xiao, W. Xu, J. Yang, X. Q. Yang, J. G. Zhang, *Nat. Energy* **2019**, *4*, 180.
- [7] S. K. Vineeth, M. Tebyetekerwa, H. Liu, C. B. Soni, N. Sungjammenla, X. S. Zhao, V. Kumar, *Mater. Adv.* **2022**, *3*, 6415.
- [8] G. Liu, J. Yang, J. Wu, Z. Peng, X. Yao, *Adv. Mater.* **2024**, *36*, 2311475.
- [9] Sungjammenla, S. K. Vineeth, V. Kumar, *Room-Temperature Sodium-Sulfur Batteries*, pp. 39–78. <https://doi.org/10.1002/9781003388067-3>.
- [10] Z. Hong, H. Maleki, T. Ludwig, Y. Zhen, M. Wilhelm, D. Lee, K. H. Kim, S. Mathur, *J. Energy Chem.* **2021**, *62*, 660.

- [11] Sungjemenla, C. B. Soni, S. K. Vineeth, V. Kumar, *Mater Adv.* **2021**, *2*, 4165.
- [12] L. Shen, J. Yang, G. Liu, M. Avdeev, X. Yao, *Mater. Today Energy* **2021**, *20*, 100691.
- [13] M. Samiee, B. Radhakrishnan, Z. Rice, Z. Deng, Y. S. Meng, S. P. Ong, J. Luo, *J. Power Sources* **2017**, *347*, 229.
- [14] A. C. Radjendirane, D. K. Maurya, J. Ren, H. Hou, H. Algadi, B. B. Xu, Z. Guo, S. Angaiah, *Langmuir* **2024**, *40*, 16690.
- [15] M. P. Fertig, K. Skadell, M. Schulz, C. Dirksen, P. Adelhelm, M. Stelter, *Batteries Supercaps* **2022**, *5*, e202100131.
- [16] S. K. Vineeth, V. Kumar, in *Room-Temperature Sodium-Sulfur Batteries* (2023), pp. 1–16. <https://doi.org/10.1201/9781003388067-1>.
- [17] K. Shi, B. Guan, Z. Zhuang, J. Chen, Y. Chen, Z. Ma, C. Zhu, X. Hu, S. Zhao, H. Dang, J. Guo, L. Chen, K. Shu, Y. Li, Z. Guo, C. Yi, J. Hu, Z. Huang, *Energy Fuels* **2024**, *38*, 9280.
- [18] X. Gao, Z. Xing, M. Wang, C. Nie, Z. Shang, Z. Bai, S. X. Dou, N. Wang, *Energy Storage Mater.* **2023**, *60*, 102821.
- [19] P. Yang, Z. Wu, Y. Liang, H. Chen, C. Lin, J. Qiu, J. Meng, Y. He, S. Zhang, *Prog. Mater. Sci.* **2025**, *154*, 101503.
- [20] S. Yang, N. Li, E. Zhao, C. Wang, J. He, X. Xiao, D. Fang, Q. Ni, X. Han, X. Xue, L. Chen, N. Li, J. Li, T. Guo, Y. Su, H. Jin, *Sci. Adv.* **10**, *2024*, 47.
- [21] F. Ling, J. Diao, Y. Yao, R. Bai, Z. Li, M. Ma, Z. Li, H. Huang, S. Zhu, X. Rui, Y. Shao, G. Henkelman, Y. Yu, *Adv. Funct. Mater.* **2025**, 2419970.
- [22] S. K. Vineeth, P. Sreram, A. Vlad, R. Joy, P. Raghavan, A. Pullanchiyodan, Elsevier, Amsterdam / New York pp. **2023**, 203.
- [23] W. Tang, R. Qi, J. Wu, Y. Zuo, Y. Shi, R. Liu, W. Yan, J. Zhang, *Electrochem. Energ. Rev.* **2024**, *7*, 23.
- [24] Y. Ji, J. Li, J. Li, *Batteries* **2022**, *8*, 157.
- [25] D. H. S. Tan, A. Banerjee, Z. Chen, Y. S. Meng, *Nat. Nanotechnol.* **2020**, *15*, 170.
- [26] Y. Gu, H. Tao, X. Yang, *Small* **2024**, *20*, 2403864.
- [27] R. Asakura, D. Reber, L. Duchêne, S. Payandeh, A. Remhof, H. Hagemann, C. Battaglia, *Energy Environ. Sci.* **2020**, *13*, 5048.
- [28] X. Yu, L. Xue, J. B. Goodenough, A. Manthiram, *Adv. Energy Sustainability Res.* **2021**, *2*, 2000061.
- [29] S. K. Vineeth, C. B. Soni, Y. Sun, V. Kumar, Z. W. Seh, *Trends Chem.* **2022**, *4*, 48.
- [30] C. B. Soni, S. K. V. Sungjemenla, V. Kumar, *Energy Storage* **2022**, *4*, e264.
- [31] M. Hou, Y. Zhou, F. Liang, H. Zhao, D. Ji, D. Zhang, L. Li, Y. Lei, *Chem. Eng. J.* **2023**, *475*, 146227.
- [32] Z. Li, P. Liu, K. Zhu, Z. Zhang, Y. Si, Y. Wang, L. Jiao, *Energy Fuels* **2021**, *35*, 9063.
- [33] X. Tang, W. Han, Y. Zhang, S. Liu, *J. Power Sources* **2024**, *623*, 235397.
- [34] X. Yu, A. Manthiram, *Acc. Chem. Res.* **2017**, *50*, 2653.
- [35] T. Famprakis, P. Canepa, J. A. Dawson, M. S. Islam, C. Masquelier, *Nat. Mater.* **2019**, *18*, 1278.
- [36] T. Liu, X. Yang, J. Nai, Y. Wang, Y. Liu, C. Liu, X. Tao, *Chem. Eng. J.* **2021**, *409*, 127943.
- [37] S. K. Vineeth, C. B. Soni, C. S. Sungjemenla, Y. Yamauchi, M. Han, V. Kumar, *J. Energy Storage* **2023**, *73*, 108780.
- [38] M. Wu, H. Liu, X. Qi, D. Li, C. Wang, C. W. Nan, L. Z. Fan, *InfoMat* **2024**, *6*, e12606.
- [39] Y. Gu, H. Ma, X. Fan, H. Tao, X. Yang, L. Z. Fan, *Adv. Funct. Mater.* **2024**, *35*, 2416077.
- [40] H. Khezraqa, M. Golshan, M. Salami-Kalajahi, *Appl. Energy* **2025**, *384*, 125509.
- [41] H. Darjazi, M. Falco, F. Colò, L. Balducci, G. Piana, F. Bella, G. Meligrana, F. Nobili, G. A. Elia, C. Gerbaldi, *Adv. Mater.* **2024**, *36*, 2313572.
- [42] Z. W. Seh, J. Sun, Y. Sun, Y. Cui, *ACS. Cent. Sci.* **2015**, *1*, 449.
- [43] K. Xu, *Chem. Rev.* **2004**, *104*, 4303.
- [44] Z. Gao, J. Yang, G. Li, T. Ferber, J. Feng, Y. Li, H. Fu, W. Jaegermann, C. W. Monroe, Y. Huang, *Adv. Energy Mater.* **2022**, *12*, 2103607.
- [45] A. Chakraborty, R. Thirupathi, S. Bhattacharyya, K. Singh, S. Omar, *J. Power Sources* **2023**, *572*, 233092.
- [46] Z. Wu, S. He, C. Zheng, J. Gan, L. She, M. Zhang, Y. Gao, Y. Yang, H. Pan, *eScience* **2024**, *4*, 100247.
- [47] J. Sang, B. Tang, Y. Qiu, Y. Fang, K. Pan, Z. Zhou, *Energy Environ. Mater.* **2023**, *7*, e12670.
- [48] C. Hänsel, P. V. Kumar, D. Kundu, *Chem. Mater.* **2020**, *32*, 10501.
- [49] Y. Uchida, G. Hasegawa, K. Shima, M. Inada, N. Enomoto, H. Akamatsu, K. Hayashi, *ACS Appl. Energy Mater.* **2019**, *2*, 2913.
- [50] T. Ortmann, T. Fuchs, J. K. Eckhardt, Z. Ding, Q. Ma, F. Tietz, C. Kübel, M. Rohrke, J. Janek, *Adv. Energy Mater.* **2024**, *14*, 2302729.
- [51] E. P. Alsaç, D. L. Nelson, S. G. Yoon, K. A. Cavallaro, C. Wang, S. E. Sandoval, U. D. Eze, W. J. Jeong, M. T. McDowell, *Chem. Rev.* **2025**, *125*, 2009.
- [52] Y. Zhao, C. Wang, Y. Dai, H. Jin, *Nano Energy* **2021**, *88*, 106293.
- [53] Q. Guo, X. Wang, M. Fu, X. Yu, J. Chen, D. Wang, C. Dong, Z. Mao, *Ceram. Int.* **2023**, *49*, 35221.
- [54] Z. Yang, L. Chen, H. Jiang, X. Liang, J. Wei, Z. Xie, B. Tang, Z. Zhou, *Adv. Funct. Mater.* **2023**, *33*, 2306558.
- [55] Z. Yao, Y. Kang, M. Hou, J. Huang, J. Zhang, B. Yang, Y. Dai, F. Liang, *Adv. Funct. Mater.* **2022**, *32*, 2111919.
- [56] D. Yang, Q. Guan, B. Wang, D. Zhang, K. Ren, H. Zhou, X. Li, Y. Zhou, Y. Cai, P. Liu, L. Zhao, M. Hou, B. Yang, D. Xue, F. Liang, *Adv. Funct. Mater.* **2024**, *35*, 2420014.
- [57] D. A. Edelman, T. G. Brandt, E. Temeche, R. M. Laine, *Mater. Today Commun.* **2022**, *32*, 104009.
- [58] W. Dong, F. Huang, *eScience* **2024**, *4*, 100158.
- [59] A. Manthiram, X. Yu, S. Wang, *Nat. Rev. Mater.* **2017**, *2*, 16103.
- [60] X. Wang, Y. Fan, J. Li, X. Li, W. Li, J. Wang, W. K. Pang, *Energy Environ. Sci.* **2024**, *17*, 1096.
- [61] C. Yuan, J. Wu, W. Zhang, M. Han, Y. Jia, *J. Energy Chem.* **2025**, *108*, 495.
- [62] J. Minkiewicz, G. M. Jones, S. Ghazizadeh, S. Bostanchi, T. J. Wasely, S. A. Yamini, V. Nekouie, *Open Ceram.* **2023**, *16*, 100497.
- [63] H. Liu, Y. Xing, N. Chen, J. Wu, Y. Li, C. Zhang, *Chem. Mater.* **2023**, *35*, 8686.
- [64] Z. Azmi, A. K. Goswami, S. R. Mohapatra, *Sustainable Mater. Technol.* **2024**, *42*, e01176.
- [65] L. Qiao, X. Judez, T. Rojo, M. Armand, H. Zhang, *J. Electrochem. Soc.* **2020**, *167*, 070534.
- [66] X. Yu, Y. Yao, X. Wang, S. Cen, D. Li, H. Ma, J. Chen, D. Wang, Z. Mao, C. Dong, *Energy Storage Mater.* **2023**, *54*, 221.
- [67] C. Che, F. Wu, Y. Li, Y. Li, S. Li, C. Wu, Y. Bai, *Adv. Mater.* **2024**, *36*, 2402291.
- [68] H. Ahmad, K. T. Kubra, A. Butt, U. Nisar, F. J. Iftikhar, G. Ali, *J. Power Sources* **2023**, *581*, 233518.
- [69] Sungjemenla, C. B. Soni, S. K. Vineeth, V. Kumar, *Adv. Energy Sustain. Res.* **2021**, *3*, 2100157.
- [70] Q. Ma, F. Tietz, *ChemElectroChem* **2020**, *7*, 2693.
- [71] S. Liu, C. Zhou, Y. Wang, W. Wang, Y. Pei, J. Kieffer, R. M. Laine, *ACS Appl. Mater. Interfaces* **2020**, *12*, 3502.
- [72] H. Fu, Q. Yin, Y. Huang, H. Sun, Y. Chen, R. Zhang, Q. Yu, L. Gu, J. Duan, W. Luo, *ACS Mater. Lett.* **2020**, *2*, 127.
- [73] D. Li, X. Wang, Q. Guo, X. Yu, S. Cen, H. Ma, J. Chen, D. Wang, Z. Mao, C. Dong, *Carbon Energy* **2023**, *5*, e299.
- [74] J. A. S. Oh, J. Sun, M. Goh, B. Chua, K. Zeng, L. Lu, *Adv. Energy Mater.* **2021**, *11*, 2101228.
- [75] K. Cao, X. Zhao, J. Chen, B. B. Xu, M. W. Shahzad, W. Sun, H. Pan, M. Yan, Y. Jiang, *Adv. Energy Mater.* **2022**, *12*, 2102579.
- [76] F. Li, M. Hou, L. Zhao, D. Zhang, B. Yang, F. Liang, *Energy Storage Mater.* **2024**, *65*, 103181.
- [77] W. Zhang, F. H. Richter, S. P. Culver, T. Leichtweiss, J. G. Lozano, C. Dietrich, P. G. Bruce, W. G. Zeier, J. Janek, *ACS Appl. Mater. Interfaces* **2018**, *10*, 22226.
- [78] H. Yamauchi, J. Ikejiri, K. Tsunoda, A. Tanaka, F. Sato, T. Honma, T. Komatsu, *Sci. Rep.* **2020**, *10*, 9453.
- [79] Z. Zhang, Q. Zhang, J. Shi, Y. S. Chu, X. Yu, K. Xu, M. Ge, H. Yan, W. Li, L. Gu, Y. S. Hu, H. Li, X. Q. Yang, L. Chen, X. Huang, *Adv. Energy Mater.* **2017**, *7*, 1601196.
- [80] M. Dixit, N. Muralidharan, A. Bisht, C. J. Jafta, C. T. Nelson, R. Amin, R. Essehlí, M. Balasubramanian, I. Belharouak, *ACS Energy Lett.* **2023**, *8*, 2356.
- [81] D. K. Singh, A. Henss, B. Mogwitz, A. Gautam, J. Horn, T. Krauskopf, S. Burkhardt, J. Sann, F. H. Richter, J. Janek, *Cell Rep. Phys. Sci.* **2022**, *3*, 101043.
- [82] P. Hu, Y. Zhang, X. Chi, K. K. Rao, F. Hao, H. Dong, F. Guo, Y. Ren, L. C. Grabow, Y. Yao, *ACS Appl. Mater. Interfaces* **2019**, *11*, 9672.
- [83] P. Pirayesh, E. Jin, Y. Wang, Y. Zhao, *Energy Environ. Sci.* **2023**, *17*, 442.
- [84] Q. Lu, A. Yang, A. Omar, Q. Ma, F. Tietz, O. Guillou, D. Mikhailova, *Energy Technol.* **2022**, *10*, 2200149.
- [85] Y. Yang, S. Yang, X. Xue, X. Zhang, Q. Li, Y. Yao, X. Rui, H. Pan, Y. Yu, *Adv. Mater.* **2024**, *36*, 2308332.
- [86] D. S. Jolly, Z. Ning, J. E. Darnbrough, J. Kasemchainan, G. O. Hartley, P. Adamson, D. E. J. Armstrong, J. Marrow, P. G. Bruce, *ACS Appl. Mater. Interfaces* **2020**, *12*, 678.
- [87] Sungjemenla, C. B. Soni, S. K. Vineeth, V. Kumar, *J. Energy Storage* **2024**, *75*, 109708.
- [88] C. Sanjaykumar, Sungjemenla, M. Chandra, C. B. Soni, S. K. Vineeth, S. Das, N. Cohen, H. Kumar, D. Mandler, V. Kumar, *J. Mater. Chem. A.* **2025**, *13*, 1420.
- [89] P. M. Sundaram, C. B. Soni, Sungjemenla, S. K. Vineeth, C. Sanjaykumar, V. Kumar, *J. Energy Storage* **2023**, *63*, 107139.

- [90] X. Chi, Y. Zhang, F. Hao, S. Kmiec, H. Dong, R. Xu, K. Zhao, Q. Ai, T. Terlier, L. Wang, L. Zhao, L. Guo, J. Lou, H. L. Xin, S. W. Martin, Y. Yao, *Nat. Commun.* **2022**, *13*, 2854.
- [91] Y. Ren, N. Hortance, J. R. McBride, K. B. Hatzell, *ACS Energy Lett.* **2021**, *6*, 345.
- [92] G. Liu, X. Sun, X. Yu, W. Weng, J. Yang, D. Zhou, R. Xiao, L. Chen, X. Yao, *Chem. Eng. J.* **2021**, *420*, 127692.
- [93] S. Kmiec, E. Ruoff, A. Manthiram, *Angew. Chem. int. Ed.* **2024**, *64*, e202416979.
- [94] A. Das, N. T. M. Balakrishnan, S. K. Vineeth, J.-H. Ahn, A. Vlad, V. Pillai, P. Raghavan, in *Advanced Technologies for Rechargeable Batteries* **2024**, pp. 1–13, <https://doi.org/10.1201/9781003310167-1>.
- [95] P. M. Sundaram, S. K. Vineeth, S. Das Adhikari, C. Sanjaykumar, P. Sennu, C. B. Soni, M. Chandra, Sungjemenla, H. Kumar, V. Kumar, *ChemComm*, **2025**, <https://doi.org/10.1039/d5cc03102h>.
- [96] S. Ohno, A. Banik, G. F. Dewald, M. A. Kraft, T. Krauskopf, N. Minafra, P. Till, M. Weiss, W. G. Zeier, *Prog. Energy* **2020**, *2*, 022001.
- [97] T. H. Hwang, D. S. Jung, J. S. Kim, B. G. Kim, J. W. Choi, *Nano Lett.* **2013**, *13*, 4532.
- [98] F. Li, K. Ren, M. Hou, M. Lin, X. Yang, Y. Zhou, S. Xiong, F. Liang, *ACS Energy Lett.* **2024**, *10*, 195.
- [99] X. Xiao, S. Yang, R. Miao, D. Fang, Y. Zhao, C. Shao, Y. Wang, C. Wang, J. Li, Y. Su, H. Jin, *Energy Storage Mater.* **2025**, *80*, 104397.
- [100] J. He, S. Yang, X. Xiao, D. Fang, R. Miao, C. Wang, L. Chen, N. Li, J. Li, Y. Su, H. Jin, *Energy Storage Mater.* **2025**, *75*, 104037.
- [101] Y. Guo, K. Liu, C. Li, D. Song, H. Zhang, Z. Wang, Y. Yan, L. Zhang, S. Dai, *Adv. Energy Mater.* **2024**, *14*, 2401504.
- [102] J. Hou, T. Zhu, G. Wang, R. Cheacharoen, W. Sun, X. Lei, Q. Yuan, D. Sun, J. Zhao, *Carbon Energy* **2024**, *6*, e628.
- [103] B. Tang, P. W. Jaschin, X. Li, S. H. Bo, Z. Zhou, *Mater. Today* **2020**, *41*, 200.
- [104] M. Shen, H. Ding, L. Fan, A. M. Rao, J. Zhou, B. Lu, *Adv. Funct. Mater.* **2023**, *33*, 2213362.
- [105] E. A. Wu, C. S. Kompella, Z. Zhu, J. Z. Lee, S. C. Lee, I. H. Chu, H. Nguyen, S. P. Ong, A. Banerjee, Y. S. Meng, *ACS Appl. Mater. Interfaces* **2018**, *10*, 10076.
- [106] J. A. S. Oh, L. He, B. Chua, K. Zeng, L. Lu, *Energy Storage Mater.* **2021**, *34*, 28.
- [107] Y. K. Liu, C. Z. Zhao, J. Du, X. Q. Zhang, A. B. Chen, Q. Zhang, *Small* **2023**, *19*, 2205315.
- [108] Y. Zhang, C. Zhang, Q. Fu, H. Zhao, Y. Lei, *Sustainable Energy Fuels* **2022**, *6*, 3527.
- [109] X. Chen, Z. Guan, F. Chu, Z. Xue, F. Wu, Y. Yu, *InfoMat* **2022**, *4*, e12248.
- [110] L. Bektaert, S. Akatsuka, N. Tanibata, F. De Proft, A. Hubin, M. H. Mamme, M. Nakayama, *J. Phys. Chem. C* **2023**, *127*, 8503.
- [111] Y. Zhang, J. Tao, C. Zhang, H. Zhao, Y. Lei, *Nanotechnology* **2022**, *33*, 295403.
- [112] Y. Wu, X. Qiu, F. Liang, Q. Zhang, A. Koo, Y. Dai, Y. Lei, X. Sun, *Appl. Catal. B* **2019**, *241*, 407.
- [113] H. A. K. Toprakci, O. Toprakci, *Energies* **2023**, *16*, 3169.
- [114] Z. Xu, J. Yang, T. Zhang, L. Sun, Y. Nuli, J. Wang, S. ichi Hirano, *Adv. Funct. Mater.* **2019**, *29*, 1901924.
- [115] W. Fang, H. Jiang, Y. Zheng, H. Zheng, X. Liang, Y. Sun, C. Chen, H. Xiang, *J. Power Sources* **2020**, *455*, 227956.
- [116] J. Yang, H. Xu, J. Wu, Z. Gao, F. Hu, Y. Wei, Y. Li, D. Liu, Z. Li, Y. Huang, *Small Methods* **2021**, *5*, 2100339.
- [117] S. Yan, C. H. Yim, J. Zhou, J. Wang, S. Abouali, E. A. Baranova, A. Weck, V. Thangadurai, A. Merati, Y. Abu-Lebdeh, *J. Phys. Chem. C* **2023**, *127*, 246411.
- [118] C. Bao, B. Wang, P. Liu, H. Wu, Y. Zhou, D. Wang, H. Liu, S. Dou, *Adv. Funct. Mater.* **2020**, *30*, 2004891.
- [119] K. Cao, Y. Xia, H. Li, H. Huang, S. Iqbal, M. Yousaf, B. B. Xu, W. Sun, M. Yan, H. Pan, Y. Jiang, *Sci. Bull.* **2024**, *69*, 49.
- [120] A. Y. S. Eng, C. B. Soni, Y. Lum, E. Khoo, Z. Yao, S. K. Vineeth, V. Kumar, J. Lu, C. S. Johnson, C. Wolverton, Z. W. Seh, *Sci. Adv.* **2022**, *8*, eabm2422.
- [121] S. K. Vineeth, Y. Y. Sungjemenla, V. Kumar, in *Room-Temperature Sodium-Sulfur Batteries*, CRC Press, Boca Raton **2023**, 79.
- [122] V. S. Kala, C. B. Soni, M. C. Sungjemenla, C. Sanjaykumar, A. Bhandari, Y. Yamauchi, M. Han, V. Kumar, *J. Mater. Chem. A: Mater.* **2025**, *13*, 19969.
- [123] A. Babu, S. K. Vineeth, R. Joy, M. J. J. Fatima, N. Gupta, P. Raghavan, in *Advanced Technologies for Rechargeable Batteries*, CRC Press, Boca Raton **2024**, 236.
- [124] C. B. Soni, S. Bera, M. C. Sungjemenla, K. V.S., S. Kumar, H. Kumar, V. Kumar, *J. Mater. Chem. A: Mater.* **2024**, *12*, 21853.
- [125] Y. Li, Z. Gao, F. Hu, X. Lin, Y. Wei, J. Peng, J. Yang, Z. Li, Y. Huang, H. Ding, *Small Methods* **2020**, *4*, 2000111.
- [126] C. B. Soni, S. K. Barik, S. K. Vineeth, B. Yadav, M. Chandra, S. C. Sungjemenla, H. Kumar, V. Kumar, *J. Mater. Chem. A: Mater.* **2025**, *13*, 6813.
- [127] B. Yadav, C. B. Soni, S. Bera, H. Kumar, V. Kumar, *Electrochim. Acta* **2024**, *507*, 145212.
- [128] C. B. Soni, N. Sungjemenla, S. K. Vineeth, C. S. Kumar, V. Kumar, *Sustainable Energy Fuels* **2023**, *7*, 1908.
- [129] Y. Zheng, L. Hu, W. Li, T. Huang, J. Ma, S. Dong, G. Cui, *ACS Energy Lett.* **2024**, *9*, 5296.
- [130] P. Jia, T. Yang, Q. Liu, J. Yan, T. Shen, L. Zhang, Y. Liu, X. Zhao, Z. Gao, J. Wang, Y. Tang, J. Huang, *Nano Energy* **2020**, *77*, 105289.
- [131] C. B. Soni, S. Vineeth, V. Kumar, *In Room-Temperature Sodium-Sulfur Batteries*, CRC Press, Boca Raton **2023**, 137.
- [132] A. G. Olabi, Q. Abbas, P. A. Shinde, M. Ali Abdelkareem, *Energy* **2023**, *266*, 126408.
- [133] Z. Zhang, J. Qian, W. Lu, C. H. Chan, S. P. Lau, J. Y. Dai, *Energy Storage Mater.* **2018**, *15*, 91.
- [134] A. Daali, X. Zhou, C. Zhao, I. Hwang, Z. Yang, Y. Liu, R. Amine, C. J. Sun, W. Otieno, G. L. Xu, K. Amine, *Nano Energy* **2023**, *115*, 108753.
- [135] Y. Zheng, L. Hu, W. Li, T. Huang, J. Ma, S. Dong, G. Cui, *ACS Energy Lett.* **2024**, *9*, 5296.
- [136] M. Fehse, A. Iadecola, L. Simonelli, A. Longo, L. Stievano, *Phys. Chem. Chem. Phys.* **2021**, *23*, 23445.
- [137] X. Lin, J. Li, *ChemElectroChem* **2023**, *10*, 2201003.
- [138] R. Zhang, Y. Wu, Z. Chen, Y. Wang, J. Zhu, X. Zhuang, *J. Mater. Chem. A: Mater.* **2023**, *11*, 19195.
- [139] A. M. Tripathi, W.-N. Su, B. J. Hwang, *Chem. Soc. Rev.* **2018**, *47*, 736.
- [140] J. Park, D. Han, J. P. Son, H. Kwak, W. Ko, C. Park, C. Lee, H. W. Lee, J. Kim, K. W. Nam, Y. S. Jung, *ACS Energy Lett.* **2024**, *9*, 2222.
- [141] Z. Wei, L. F. Nazar, J. Janek, *Batteries Supercaps* **2024**, *7*, e202400005.
- [142] A. Sivakumaran, A. J. Samson, V. Thangadurai, *Energy Technol.* **2023**, *11*, 2201323.
- [143] L. Xu, S. Tang, Y. Cheng, K. Wang, J. Liang, C. Liu, Y. C. Cao, F. Wei, L. Mai, *Joule* **2018**, *2*, 1991.
- [144] M. C. Bay, M. Wang, R. Grissa, M. V. F. Heinz, J. Sakamoto, C. Battaglia, *Adv. Energy Mater.* **2020**, *10*, 1902899.
- [145] Q. Ma, T. Ortmann, A. Yang, D. Sebold, S. Burkhardt, M. Rohnke, F. Tietz, D. Fattakhova-Rohlfing, J. Janek, O. Guillou, *Adv. Energy Mater.* **2022**, *12*, 2201680.
- [146] W. Wang, S. Hu, Z. Liu, Z. Jian, W. Chen, *J. Phys. Chem. Solids* **2023**, *178*, 111365.
- [147] A. Hayashi, K. Noi, N. Tanibata, M. Nagao, M. Tatsumisago, *J. Power Sources* **2014**, *258*, 420.
- [148] Z. Yu, S. L. Shang, J. H. Seo, D. Wang, X. Luo, Q. Huang, S. Chen, J. Lu, X. Li, Z. K. Liu, D. Wang, *Adv. Mater.* **2017**, *29*, 1605561.
- [149] H. Gamo, H. H. P. Nguyen, R. Matsuda, H. Muto, A. Matsuda, *Solid State Ion* **2020**, *344*, 115133.
- [150] X. Miao, H. Wang, R. Sun, X. Ge, D. Zhao, P. Wang, R. Wang, L. Yin, *Adv. Energy Mater.* **2021**, *11*, 2003469.
- [151] E. Matios, H. Wang, C. Wang, X. Hu, X. Lu, J. Luo, W. Li, *ACS Appl. Mater. Interfaces* **2019**, *11*, 5064.
- [152] J. Yang, Z. Gao, T. Ferber, H. Zhang, C. Guhl, L. Yang, Y. Li, Z. Deng, P. Liu, C. Cheng, R. Che, W. Jaegermann, Y. H. Renéhausbrand, *J. Mater. Chem. A: Mater.* **2020**, *8*, 7828.
- [153] X. Wang, J. Chen, D. Wang, Z. Mao, *Nat. Commun.* **2021**, *12*, 7109.
- [154] J. A. S. Oh, Y. Wang, Q. Zeng, J. Sun, Q. Sun, M. Goh, B. Chua, K. Zeng, L. Lu, *J. Colloid Interface Sci.* **2021**, *601*, 418.
- [155] Y. Lu, J. A. Alonso, Q. Yi, L. Lu, Z. L. Wang, C. Sun, *Adv. Energy Mater.* **2019**, *9*, 1901205.
- [156] P. Jiang, G. Du, Y. Shi, F. She, P. Guo, G. Qian, X. Lu, F. Xie, X. Lu, *Chem. Eng. J.* **2023**, *451*, 138771.
- [157] C. Wang, H. Jin, Y. Zhao, *Small* **2021**, *17*, 2100974.
- [158] C. Peng, S. Huang, X. Shen, J. Ding, J. Luo, J. Du, Z. Xia, X. Zhang, J. Chen, *J. Mater. Chem. A: Mater.* **2024**, *12*, 23485.
- [159] C. Fu, Y. Li, W. Xu, X. Feng, W. Gu, J. Liu, W. Deng, W. Wang, A. M. M. Abeykoon, L. Su, L. Zhu, X. Wu, H. Xiang, *Nat. Commun.* **2024**, *15*, 2402891.
- [160] B. Xun, J. Wang, Y. Sato, S. Jia, S. Ohno, H. Akamatsu, K. Hayashi, *Adv. Energy Mater.* **2024**, 2402891.
- [161] H. Li, Z. Zhang, B. Liu, J. Liu, B. Chen, J. Zhou, *Comput. Mater. Sci.* **2023**, *216*, 111848.

- [162] L. Yu, Q. Jiao, B. Liang, H. Shan, C. Lin, C. Gao, X. Shen, S. Dai, *J. Alloys Compd.* **2022**, *913*, 165229.
- [163] M. D. Singh, D. K. Gorai, K. Brajesh, P. Singh, V. Ranawade, A. V. Shinde, M. Jarer, R. Gupta, A. Garg, V. Agarwal, K. S. Nalwa, *Chem. Eng. J.* **2024**, *489*, 151330.
- [164] X. Wang, J. Chen, Z. Mao, D. Wang, *Chemical Engineering Journal* **2022**, *427*, 130899.
- [165] P. Yang, Z. Wu, M. Li, C. Zhang, Y. Wang, Y. Zhu, M. Li, Y. Wang, D. sheng Li, H. Chen, S. Zhang, *Angew. Chem. Int. Ed.* **2024**, *137*, e202417778.
- [166] T. Dai, S. Wu, Y. Lu, Y. Yang, Y. Liu, C. Chang, X. Rong, R. Xiao, J. Zhao, Y. Liu, W. Wang, L. Chen, Y. S. Hu, *Nat. Energy* **2023**, *8*, 1221.
- [167] S. He, Y. Xu, Y. Chen, X. Ma, *J. Mater. Chem. A: Mater.* **2020**, *8*, 12594.
- [168] A. Hayashi, K. Noi, A. Sakuda, M. Tatsumisago, *Nat. Commun.* **2012**, *3*, 856.
- [169] A. Banerjee, K. H. Park, J. W. Heo, Y. J. Nam, C. K. Moon, S. M. Oh, S. Hong, Y. S. Jung, *Angew. Chem.* **2016**, *128*, 9786.
- [170] Z. L. Dong, Y. Yuan, V. Martins, E. Jin, Y. Gan, X. Lin, Y. Gao, X. Hao, Y. Guan, J. Fu, X. Pang, Y. Huang, Q. H. Tu, T. K. Sham, Y. Zhao, *Nano Energy* **2024**, *128*, 109871.
- [171] C. K. Moon, H. J. Lee, K. H. Park, H. Kwak, J. W. Heo, K. Choi, H. Yang, M. S. Kim, S. T. Hong, J. H. Lee, Y. S. Jung, *ACS Energy Lett.* **2018**, *3*, 2504.
- [172] X. Zhang, K. C. Phuah, S. Adams, *Chem. Mater.* **2021**, *33*, 9184.
- [173] X. Feng, P. H. Chien, Z. Zhu, I. H. Chu, P. Wang, M. Immediato-Scuotto, H. Arbabzadeh, S. P. Ong, Y. Y. Hu, *Adv. Funct. Mater.* **2019**, *29*, 1807951.
- [174] C. Wang, Z. Sun, Y. Zhao, B. Wang, C. Shao, C. Sun, Y. Zhao, J. Li, H. Jin, L. Qu, *Small* **2021**, *17*, 2103819.
- [175] Q. Ma, M. Guin, S. Naqash, C. L. Tsai, F. Tietz, O. Guillou, *Chem. Mater.* **2016**, *28*, 4821.
- [176] Z. Huang, S. Yoshida, H. Akamatsu, K. Hayashi, S. Ohno, *ACS Mater. Lett.* **2024**, *6*, 1732.
- [177] X. Y. Niu, X. Y. Dou, C. Y. Fu, Y. C. Xu, X. Y. Feng, *RSC Adv.* **2024**, *14*, 14716.
- [178] T. Zhao, A. N. Sobolev, R. Schlem, B. Helm, M. A. Kraft, W. G. Zeier, *ACS Appl. Energy Mater.* **2023**, *6*, 4334.
- [179] G. Sun, C. Lou, B. Yi, W. Jia, Z. Wei, S. Yao, Z. Lu, G. Chen, Z. Shen, M. Tang, F. Du, *Nat. Commun.* **2023**, *14*, 6501.
- [180] J. K. Kim, Y. J. Lim, H. Kim, G. B. Cho, Y. Kim, *Energy Environ. Sci.* **2015**, *8*, 3589.
- [181] H. Lai, J. Wang, M. Cai, Z. Song, X. Gao, X. Wu, Z. Wen, *Chem. Eng. J.* **2022**, *433*, 133545.
- [182] D. Xu, H. Jiang, M. Li, O. Hai, Y. Zhang, *Ceram. Int.* **2015**, *41*, 5355.
- [183] G. Chen, J. Lu, X. Zhou, L. Chen, X. Jiang, *Ceram. Int.* **2016**, *42*, 16055.
- [184] E. Yi, E. Temeche, R. M. Laine, *J. Mater. Chem. A: Mater.* **2018**, *6*, 12411.
- [185] L. Ran, A. Baktash, M. Li, Y. Yin, B. Demir, T. Lin, M. Li, M. Rana, I. Gentle, L. Wang, D. J. Searles, R. Knibbe, *Energy Storage Mater.* **2021**, *40*, 282.
- [186] J. Wu, H. Liu, Y. Li, C. Zhang, *Chem. Commun.* **2023**, *59*, 8985.
- [187] S. Cai, H. Tian, J. Liu, S. Liu, L. Dai, J. Xu, L. Kong, L. Wang, *J. Mater. Chem. A: Mater.* **2022**, *10*, 1284.
- [188] X. Miao, H. Di, X. Ge, D. Zhao, P. Wang, R. Wang, C. Wang, L. Yin, *Energy Storage Mater.* **2020**, *30*, 170.
- [189] Q. Zhang, F. Liang, T. Qu, Y. Yao, W. Ma, B. Yang, Y. Dai, in *IOP Conf Ser Mater Sci Eng*, Vol. 57, Institute of Physics Publishing, 393001.
- [190] V. M. Pratiwi, L. Noerochim, H. Purwaningsih, A. A. Wibowo, F. A. Maulana, *Eng. Chem.* **2024**, *5*, 43.
- [191] D. Zhang, X. Cao, D. Xu, N. Wang, C. Yu, W. Hu, X. Yan, J. Mi, B. Wen, L. Wang, L. Zhang, *Electrochim. Acta* **2018**, *259*, 100.
- [192] W. D. Richards, T. Tsujimura, L. J. Miara, Y. Wang, J. C. Kim, S. P. Ong, I. Uechi, N. Suzuki, G. Ceder, *Nat. Commun.* **2016**, *7*, 11009.
- [193] S. H. Bo, Y. Wang, J. C. Kim, W. D. Richards, G. Ceder, *Chem. Mater.* **2016**, *28*, 252.
- [194] Q. Ma, J. Liu, X. Qi, X. Rong, Y. Shao, W. Feng, J. Nie, Y. S. Hu, H. Li, X. Huang, L. Chen, Z. Zhou, *J. Mater. Chem. A: Mater.* **2017**, *5*, 7738.
- [195] Y. Zheng, Q. Pan, M. Clites, B. W. Byles, E. Pomerantseva, C. Y. Li, *Adv. Energy Mater.* **2018**, *8*, 1801885.
- [196] C. Sængeland, R. Mogensen, D. Brandell, J. Mindemark, *ACS Appl. Polym. Mater.* **2019**, *1*, 825.
- [197] S. Chen, F. Feng, Y. Yin, H. Che, X. Z. Liao, Z. F. Ma, *J. Power Sources* **2018**, *399*, 363.

Manuscript received: May 28, 2025

Revised manuscript received: July 6, 2025

Version of record online:
